Synoptic Modulation of the West African Coastal Atmosphere and Mesoscale Convective Systems

NAOKO SAKAEDA,[a] SHUN-NAN WU,[a] ROSIMAR RIOS-BERRIOS,[b] ELINOR MARTIN,[a] KELLY M. NÚÑEZ OCASIO,[c] KRISTOPHER M. BEDKA,[d] MARGARET HOLLIS,[a] BJORN LAMBRIGTSEN,[e] QUINTON A. LAWTON,[b] AMIN NEHRIR,[d] MANIKANDAN RAJAGOPAL,[f] MATHIAS SCHREIER,[e] K. LEE THORNHILL,[d] AND SUN WONG[e]

[a] *School of Meteorology, University of Oklahoma, Norman, Oklahoma*
[b] *NSF National Center for Atmospheric Research, Boulder, Colorado*
[c] *Department of Atmospheric Sciences, Texas A&M University, College Station, Texas*
[d] *NASA Langley Research Center, Hampton, Virginia*
[e] *NASA Jet Propulsion Laboratory, California Institute of Technology, Pasadena, California*
[f] *Department of Atmospheric Sciences, University of Utah, Salt Lake City, Utah*

(Manuscript received 20 December 2024, in final form 14 April 2025, accepted 12 June 2025)

ABSTRACT: This study uses high-resolution airborne data from the NASA Convective Process Experiments–Cabo Verde field campaign to examine the effects of synoptic conditions on mesoscale convective systems (MCSs) over the western coastal waters of West Africa. African easterly waves (AEWs) are the dominant source of synoptic variability over the region, but their influences on coastal areas remain unclear. This study compares airborne data from 2 days with contrasting synoptic conditions and MCS evolution over the coastal water. On one day, large MCSs with high rain rates persisted over the coastal water when the AEW trough was near the coastline. The flow modulation by the AEW strengthened the near-surface onshore flow and warmed and moistened the boundary layer over the coastal water. These combined effects increased the equivalent potential temperature of inflow air into the coastal MCSs, likely supporting their development. On the other day, an AEW was absent or weak, and coastal MCSs remained small and short lived without the effects of the AEW. The observed modulation of the coastal atmosphere and MCSs by AEWs during the field campaign is analogous to the historical relationship of AEW and coastal MCSs obtained by satellite and reanalysis data. Although not represented by the two field campaign cases, the historical analysis suggests the enhancement of coastal vertical wind shear by AEWs can also intensify coastal MCSs. These results highlight the importance of synoptic modulation in understanding the variability and mechanism of coastal MCSs, which differ from those over land or open ocean.

KEYWORDS: Africa; Coastlines; Tropics; Deep convectionTropical variability

1. Introduction

West Africa is a major monsoonal region that accounts for a high fraction of global seasonal rainfall, particularly over coastal waters (Biasutti et al. 2012; Houze et al. 2015; Ogino et al. 2016). Over the West African monsoon region, the maximum climatological rainfall is seen immediately offshore (within ~200 km) of its western coastline (Hamilton et al. 2017; Wu et al. 2024). This coastal offshore area has a large day-to-day variability in the amount of rainfall and associated convective activity, implying the important contribution from the skewed occurrence of mesoscale convective systems (MCSs) to the climatological rainfall (Zuluaga and Houze 2015; Hamilton et al. 2017). Furthermore, numerical simulations struggle to capture convective processes at the land–maritime transition zones, even for storm-resolving convection-permitting models (Kouadio et al. 2020; Tao et al. 2023). To understand processes relevant to convective activity around the coastline, this study focuses on examining the coupling between the coastal environment and convective activity over the western coastal waters of West Africa. This objective is achieved through integrating global satellite, reanalysis datasets, and unique airborne observations collected by the NASA Convective Process Experiments–Cabo Verde (CPEX-CV) field campaign (Nowottnick et al. 2024).

Convective systems and associated rainfall have unique properties over the coastal waters of monsoon regions that appear as the merger of their distinct characteristics between the continental and maritime regimes. Continental convective systems contain deeper and wider convective cores, while maritime convective systems contain a higher fraction of stratiform rain with shallower and narrower deep convective cores (Nesbitt et al. 2000; Schumacher and Houze 2006; Futyan and Del Genio 2007; Guy and Rutledge 2012; Houze et al. 2015; Takahashi et al. 2023). Over the western coast of West Africa, the high occurrence of wide, deep convective cores over the continent extends into the coastal waters. At the same time, the stratiform fraction over the east Atlantic Ocean is higher over the coastal waters than farther offshore (Houze et al. 2015; Zuluaga and Houze 2015). Therefore, the western coastal waters of West Africa have the unique combination of both intense deep convection and high stratiform rain, which describes the high cumulative rainfall over the coastal waters (Wu et al. 2024). The unique convective properties of this region also relate to the occurrence of regional extreme rainfall events that are both intense and extensive in size, which are only seen over the coastal waters of global monsoon regions

Corresponding author: Naoko Sakaeda, nsakaeda@ou.edu

DOI: 10.1175/MWR-D-24-0281.1

© 2025 American Meteorological Society. This published article is licensed under the terms of the default AMS reuse license. For information regarding reuse of this content and general copyright information, consult the AMS Copyright Policy (www.ametsoc.org/PUBSReuseLicenses).

Unauthenticated | Downloaded 10/23/26 03:43 PM UTC

(Hamada et al. 2014). The intense and extensive rainfall events over the coastal waters of West Africa are partly attributed to continental MCSs that transition their properties as they move offshore (Wu et al. 2024).

During the NASA African Monsoon Multidisciplinary Analysis (NAMMA) field campaign (August–September 2006), a radar was deployed at the West African coast in Senegal, which revealed how convective systems transition as they propagate offshore (Redelsperger et al. 2006; Jenkins et al. 2010). Those studies showed that deep convection typically rapidly weakens and the stratiform rain area expands as the MCSs cross the coastline due to a less favorable environment offshore than on coastal land (DeLonge et al. 2010; Guy et al. 2011; DeLonge and Fuentes 2012; Klotz and Kucera 2012). However, when the trough of African easterly waves (AEWs) is near the coastline, large coastal MCSs can develop and grow offshore (DeLonge et al. 2010; Guy et al. 2011; Dieng et al. 2014). While these offshore-propagating MCSs may generate extreme rainfall around the coastline, their occurrence is infrequent (about once every 4–5 days) (Wu et al. 2024). MCSs form more frequently over the coastal waters (once every 2–3 days), contributing to the high cumulative rainfall in the region (Wu et al. 2024). These studies indicate a wide range of MCS evolution around the coastline, where multiscale phenomena may influence MCS activity, such as the African easterly jet, Saharan dust, and AEWs (Diallo et al. 2013; Bercos-Hickey et al. 2020; Núñez Ocasio et al. 2021).

Over West Africa and during boreal summer, AEWs are the dominant sources of synoptic-scale variability that strongly influence convective activity and subsequent Atlantic cyclogenesis (Berry and Thorncroft 2005; Hopsch et al. 2010; Janiga and Thorncroft 2016; Núñez Ocasio and Rios-Berrios 2023). Previous studies have demonstrated that AEWs modulate the occurrence of rainfall and MCSs differently depending on the region (Kiladis et al. 2006; Pereira and Rutledge 2006; Janiga and Thorncroft 2016; Schwendike and Jones 2010; Russell and Aiyyer 2020; Fischer et al. 2024). Over central and eastern Africa, more rainfall occurs west of AEW troughs due to strong adiabatic forcing associated with anomalous northerlies (Fink and Reiner 2003; Janiga and Thorncroft 2016). However, rainfall is enhanced within AEW troughs over the eastern Atlantic basin due to enhanced moisture. Despite the well-known difference in AEW–MCS relationships between land and ocean, less attention has been paid to their relationship over the coastal area.

Within the limited studies, some disagreement and uncertainty remain on how AEWs influence MCSs around the coastline (Guy et al. 2011; Klotz and Kucera 2012; Dieng et al. 2014; Hamilton et al. 2017; Zuluaga and Houze 2015). For example, while Guy et al. (2011) concluded that the frequency of coastal MCSs is insensitive to AEWs during the NAMMA period, Janiga and Thorncroft (2016) showed a strong coastal rainfall variability with AEWs using satellite observations and reanalysis over 15 years. When AEW troughs are near the coastline, MCSs tend to grow larger and intensify as they propagate offshore, but the reason has been attributed to different thermodynamic and kinematic properties, such as humidity and vertical wind shear (Guy et al. 2011; Dieng et al. 2014). Given these uncertainties and that the interactions between AEWs and MCSs influence the subsequent chance of tropical cyclogenesis associated with AEWs (Schwendike and Jones 2010; Klotz and Kucera 2012; Núñez Ocasio et al. 2020), it is important to improve our understanding of coastal interactions between AEWs and convection.

One of the challenges in understanding coastal convection and its modulation by AEWs comes from the lack of three-dimensional observations of the atmosphere in the region. This gap in observations is addressed by the unique measuring capabilities of airborne observations from the NASA CPEX-CV field campaign, which captured varying synoptic and convective conditions over the western coastal water of West Africa. This study will highlight new observational insights on the synoptic environmental control of coastal convection from the field campaign, reanalysis, and satellite data.

2. Data and methods

Broad science objectives of NASA CPEX-CV included improving understanding of interactions among convective cloud systems, aerosols, boundary layer kinematic and thermodynamic conditions, and large-scale environmental forcings, such as AEWs, the ITCZ, and Saharan air layer (Nowottnick et al. 2024). To achieve these objectives, the NASA DC-8 aircraft flew from Sal, Cabo Verde, around the east Atlantic Ocean, collecting three-dimensional atmospheric, cloud, and aerosol data with remote sensing instruments, in situ probes, and dropsondes. Other ground-based measurements were taken from Cabo Verde in coordination with the Joint Aeolus Tropical Atlantic Campaign (JATAC; Borne et al. 2024), but this study focuses on maritime observations collected from research flights. Among the thirteen flight missions completed during the field campaign in September 2022, this study focuses on the flights on 20 and 22 September that captured convective systems and their environment in the western coastal waters of West Africa. Both of these flights occurred around 0500–1000 UTC (local solar time around 0400–0900), providing the comparison at the same time of day when the coastal offshore convection tends to be most active (Wu et al. 2024).

a. Airborne measurements during CPEX-CV

The three remote sensing instruments onboard DC-8 used in this study were the Doppler Aerosol Wind (DAWN) lidar (Kavaya et al. 2014; Bedka et al. 2021), the High-Altitude Lidar Observatory (HALO; Carroll et al. 2022), and the High-Altitude Monolithic Microwave Integrated Circuit Sounding Radiometer (HAMSR; Brown et al. 2011). These instruments collectively provide high-resolution profiles of clouds, aerosols, atmospheric kinematics, and thermodynamics along and below flight tracks within the optimal conditions for the instruments. DAWN provides horizontal wind speed and directions at 66-m vertical and approximately 4-km horizontal resolutions. HALO provides water vapor mixing ratio, aerosol, and cloud optical properties at 315–585-m vertical and 2–12-km horizontal spacing for water vapor and 15-m vertical and ~2-km horizontal spacing for aerosol backscatter. These retrievals from DAWN and HALO were limited to clear or

Unauthenticated | Downloaded 10/23/26 03:43 PM UTC

optically thin cloudy conditions. This limitation does not apply to HAMSR, which provides temperature and water vapor profiles in cloudy or lightly precipitating conditions at 1–2-km vertical and 1–2-km horizontal spacing. However, HAMSR data around precipitating clouds must be interpreted cautiously, as we found some near-surface moist and warm biases can appear compared to dropsonde data (not shown).

In addition to the remote sensing instruments, dropsondes were launched about every 5–10 min (about 75–125 km) along the flight track, depending on the sampling targets. The dropsondes provide vertical profiles of thermodynamic and kinematic variables in all conditions, supplementing data in cloudy conditions when the lidar retrievals were limited. Cloud layers that dropsondes have gone through are checked by identifying layers with 100% relative humidity. No dropsonde data in this study have cloud layers thicker than 1 km. Given the thin layers of clouds and their minimal impacts, data within cloud layers are included in the thermodynamic variables shown later. Thermodynamic variables evaluated from dropsondes include CAPE and CIN. Flight altitudes varied around 8–12 km, which were mostly below the level of neutral buoyancy. To facilitate a consistent comparison of CAPE from dropsondes initiated at varying altitudes, its calculation was kept below 400 hPa. CAPE and CIN calculations include a 10% km^{-1} entrainment rate following Molinari et al. (2012) to account for processes that reduce parcel buoyancy and that are not considered in traditional undiluted CAPE calculations. The entraining CAPE and CIN are used to assess environmental influences on buoyancy and its relation to coastal convection.

To facilitate the comparison of all data, HAMSR data were converted from the original isobaric to Cartesian height coordinates using the hydrostatic equation. This choice was made because DAWN and HALO could not be converted to isobaric coordinates due to the lack of pressure information at their resolutions. Therefore, part of the discrepancy in temperature and water vapor measurements between HAMSR and other instruments may result from the invalidity of pure hydrostatic balance assumption. However, this caveat does not influence the overall conclusions of this study.

b. Other data

To examine the spatiotemporal distribution of rainfall, we use the Integrated Multi-satellitE Retrievals for Global Precipitation Measurement (IMERG), version 7 (Huffman et al. 2024), that provides global rainfall estimates through a multisatellite gauge combination of data at 30-min temporal and 0.1° horizontal grid spacing. We describe in section 2c how the MCS tracking algorithm is applied to this dataset.

To supplement the limited samples of DC-8 data, we also use MERRA-2 reanalysis to examine synoptic conditions around the western coast of West Africa. From MERRA-2 products, we use 3-hourly instantaneous three-dimensional meteorological fields at 0.5° latitude × 0.625° longitude grid spacing on 42 isobaric levels from 1 to 1000 hPa (Gelaro et al. 2017). We have also checked the sensitivity of our results to using ERA5 reanalysis (Hersbach et al. 2020). Some differences appear between the reanalyses as expected, especially in the boundary layer, but the overall conclusions are insensitive to the choice of reanalyses.

c. Tracking algorithms of MCSs and AEWs

To understand the life cycle of convective systems observed by the research flights, we use the Tracked IMERG Mesoscale Precipitating Systems (TIMPS; Rajagopal et al. 2023). TIMPS applies the forward-in-time (FiT) tracking algorithm (Skok et al. 2013) to smoothed IMERG precipitation fields. It first identifies precipitation features at each time by finding precipitation maxima and expanding the feature to neighboring precipitation pixels. The FiT algorithm then links the precipitation features in consecutive time steps using the overlapping method to identify time-evolving "tracked precipitation systems." If a system splits into multiple features, they are still tracked as the same system if their centroids are less than 200 km apart; otherwise, they are tracked as separate systems. If multiple tracked systems merge into one, it follows the track of the largest of the merged features, and the tracks of smaller features are terminated. Among the tracked precipitation systems, MCSs are identified as systems that last for 6 or more hours, reach at least 3000 km^2 in area, and contain rain rates exceeding 10 mm h^{-1} at some point in their lifetime. The location of the tracked MCSs is calculated using the centroid of precipitating features, weighted by IMERG precipitation.

Climatological MCS frequency and characteristics are known to be sensitive to the choice of tracking algorithms (Feng et al. 2025; Prein et al. 2024). However, our study focuses on synoptic variability of MCS frequency and characteristics from their climatological averages, reducing the known sensitivity to tracking algorithms. Wu et al. (2024) used TIMPS to document the climatological frequency and evolution of MCSs around the western coast of West Africa, which appear qualitatively consistent with other previously documented MCS statistics (Roca et al. 2017; Feng et al. 2021; Takahashi et al. 2021). We chose to use TIMPS to make our study comparable with Wu et al. (2024), but the sensitivity of our results to MCS tracking algorithms remains to be determined in a future study.

We use global tracks of tropical easterly waves (Hollis et al. 2024) to identify the amplitude and location of AEW troughs around West Africa. This dataset tracks all tropical easterly waves using MERRA-2 850- and 700-hPa cyclonic curvature vorticity. Following the TRACK algorithm of Hodges (1995), it first identifies contiguous areas of curvature vorticity above 1×10^{-5} s^{-1} in the Northern Hemisphere (below -1×10^{-5} s^{-1} in the Southern Hemisphere). These areas of cyclonic curvature vorticity are tracked in time as the same system when they overlap in areas between time steps. The tracks that originate equatorward of 40° north or south, last for at least 2 days, and propagate westward for 15° in longitude or more are retained as tropical easterly waves. Among all the tropical easterly waves around the globe, those around West Africa are considered AEWs.

We checked the consistency of these global tropical easterly wave tracks with another tracking system that exclusively focuses on easterly waves around West Africa and the eastern Atlantic (Lawton et al. 2022). We find that the number of

Unauthenticated | Downloaded 10/23/26 03:43 PM UTC

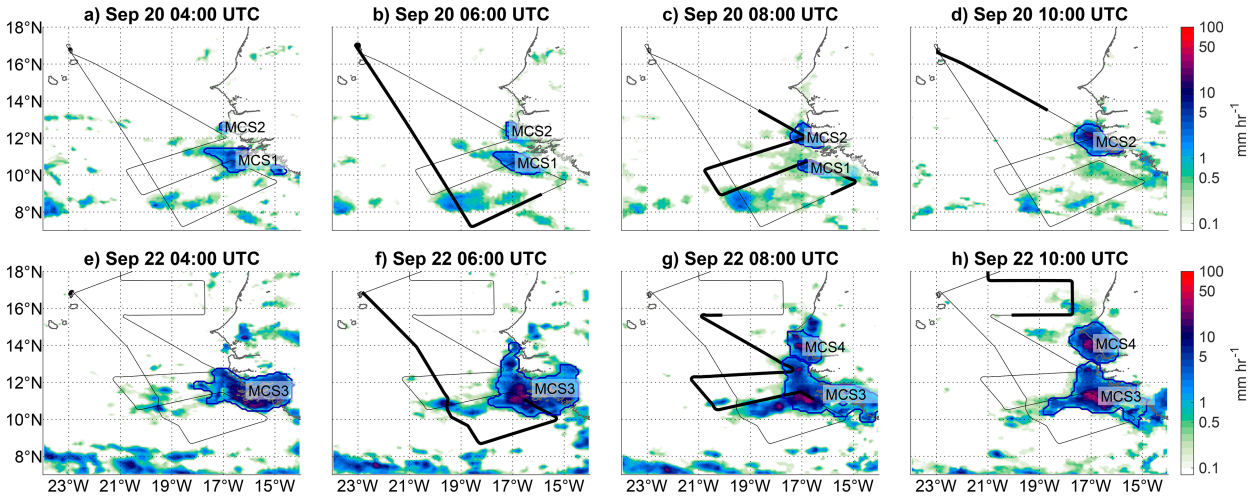


FIG. 1. IMERG rainfall rate (mm h^{-1}) at 0400, 0600, 0800, and 1000 UTC (a)–(d) 20 Sep and (e)–(h) 22 Sep. Thin lines show the full flight tracks, and thick black lines highlight those within ±1 h of the shown times. MCSs that are discussed in this study are outlined and labeled from MCS1 to MCS4.

AEWs is sensitive to the choice of tracking algorithm in part due to differences in the applied threshold of cyclonic curvature vorticity, but they agree on the tracks of strong AEWs observed during CPEX-CV (not shown). These two AEW tracks also agree on the existence and location of AEW during the two research flights of our focus. Overall conclusions on how AEWs modulate MCSs in our study region are also insensitive to the choices of AEW tracks. Therefore, we present the results using the global tropical easterly wave track using 700-hPa curvature vorticity from Hollis et al. (2024).

3. Evolution of precipitation and synoptic conditions during the two research flights

Contrasting convective activity occurred on 20 and 22 September when the two research flights (RFs) focused on convective systems near the coastline. MCSs occurred near the coastline on both days, but their properties and evolution differed (Fig. 1). On 20 September (RF 8), two small MCSs (MCS1 and MCS2 in Figs. 1a–d) formed in the morning hours over the coastal waters. MCS1 persisted for only a few hours, reaching its maximum size of about 5000 km^2. MCS2 grew to about 20 000 km^2 in size until midday on 20 September, which is about the climatological average size of MCSs that form over these coastal waters (Wu et al. 2024). In contrast, larger, longer-lasting MCSs (MCS3 and MCS4 in Figs. 1e–h) appeared on 22 September (RF 9), and both reached their maximum sizes close to 100 000 km^2 over the coastal water. MCS3 formed inland on 20 September and moved offshore around 0200 UTC 22 September, and then, it remained quasi-stationary over the coastal waters until around 1500 UTC of that day. MCS4 formed over the coastal area around 0600 UTC 22 September and grew as it moved offshore a few hours later. MCS4 moved northward and persisted near the coastline the following day, eventually forming Tropical Storm Hermine east of Cabo Verde.

The environment around the coast was likely influenced by a nearby AEW trough on 22 September but not on 20 September. Figure 2b shows that some positive curvature vorticity was present near the coastline on both 20 and 22 September, while the magnitude differed. The vorticity around the coastline on 20 September is not identified as an AEW trough due to its low magnitude and short duration by either the AEW tracking algorithm. However, another AEW trough existed farther offshore at around 28°–30°W on 20 September, which had no apparent direct influence on the coastal environment. In contrast, stronger curvature vorticity moved offshore around 22 September, identified as an AEW trough by both tracking algorithms. The strong magnitude of this AEW trough is also marked by enhanced moisture and rainfall around the coastline (Fig. 2). Therefore, 20 and 22 September provide contrasting examples of the days without and with, respectively, the impact of nearby strong AEW troughs on coastal convective systems.

On 20 September, a weak trough appeared inland (Figs. 3a,b), corresponding to the weak coastal curvature vorticity in Fig. 2b. On this day, we see the expected monsoon onshore flow and zonally elongated near-surface convergence along the ITCZ latitude around 8°–10°N (Fig. 3a). At the same time, column water vapor was higher along the ITCZ convergence zone and the coastline. These surface convergence and high column moisture conditions near the coastline appear climatologically (not shown), which may generally support the frequent formation of MCSs in this region (Wu et al. 2024).

On 22 September, the strong AEW trough was near the coastline and apparently modulated the monsoon onshore flow, surface convergence, and moisture over the coastal waters (Fig. 3b). The presence of the AEW trough is apparent from the closed streamlines at 700 hPa around the coastline (Fig. 3d). This AEW trough likely enhanced monsoon onshore flow and shifted the surface convergence northward to

Unauthenticated | Downloaded 10/23/26 03:43 PM UTC

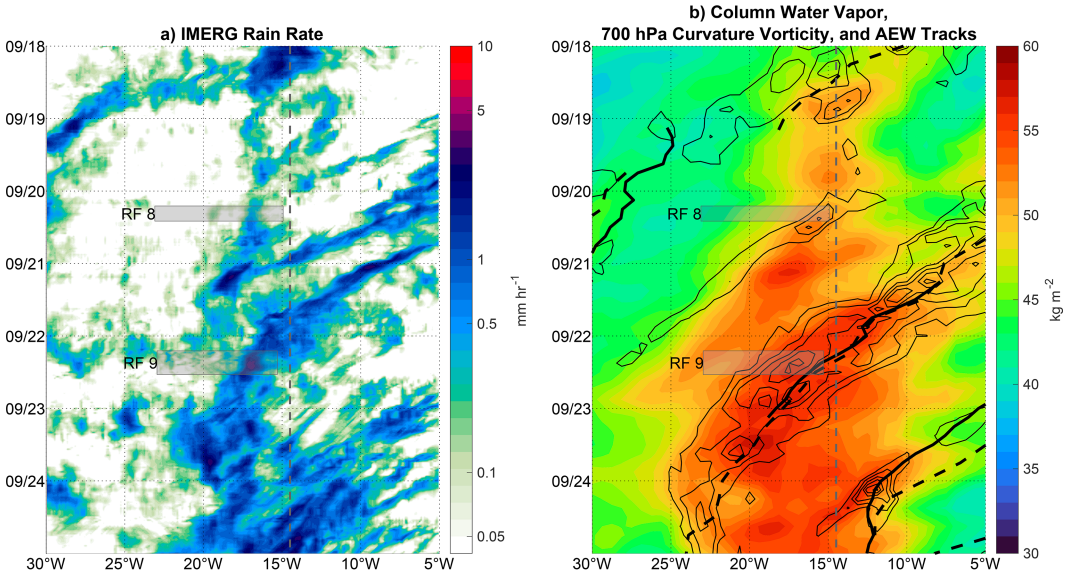


FIG. 2. 5°–20°N averaged (a) IMERG rain rate (shaded; mm h^{-1}), (b) MERRA-2 column-integrated water vapor (shaded; kg), and 700-hPa curvature vorticity (contoured every 0.5×10^{-5} s^{-1} for positive values only). Thick black solid and dashed lines in (b) show AEW tracks based on the algorithm of Hollis et al. (2024) and Lawton et al. (2022), respectively, applied to MERRA-2 700-hPa curvature vorticity. The time and longitude width of RF 8 and 9 flight tracks are shown in gray boxes. Gray dashed lines around 14.5°W show the average coastline at plotted latitudes.

about 10°–12°N near the coastline. To the north of 12°N, the lower-tropospheric easterly and northeasterly flow associated with this AEW trough also contributed to a major dust outbreak to the offshore area east of Cabo Verde, while the coastal waters remained moist at the south side of the AEW trough center (Nowottnick et al. 2024; Burgess and Oyola-Merced 2024). The dry air associated with this dust outbreak is underestimated in MERRA-2 compared to dropsondes, particularly around 12°N and 20°W. The comparison between 20 and 22 September demonstrates the apparent influences of AEW on the synoptic thermodynamic and kinematic conditions, which may have contributed to the different evolution of MCSs.

Previous studies have also documented that MCSs over the western coast and offshore of West Africa are enhanced when AEW troughs are slightly to the east of the coastline (Klotz and Kucera 2012; Dieng et al. 2014; Zuluaga and Houze 2015; Janiga and Thorncroft 2016; Hamilton et al. 2017). When AEW troughs are near the coastline, they enhance humidity and surface convergence, as seen on 22 September. However, the previous studies have relied on reanalysis data, which have high uncertainty in the tropical marine boundary layer (Wolding et al. 2022). Therefore, we next use airborne data to reassess the environment over the coastal waters with and without a strong AEW and how it relates to convective activity.

4. Airborne measurements of atmospheric profiles around coastal offshore MCSs

This section uses airborne data from 20 and 22 September to examine the high-resolution vertical structure of the atmosphere over the coastal waters. This section demonstrates that different synoptic thermodynamic and kinematic conditions on the two days influenced the marine boundary layer that relates to different MCS activity on the 2 days.

a. Observed differences in atmospheric thermodynamic and kinematic profiles between 20 and 22 September

The synoptic differences between 20 and 22 September, as discussed in section 3, contributed to different amounts and distributions of dust and associated thermodynamic conditions. The HALO data show the difference in the amount of aerosol optical thickness (AOT) and backscatter coefficients along the north–south cross section of the two research flights (Fig. 4). While a high AOT value (~1) extends to about 11°N on 22 September, AOT remains below 0.25 throughout the flight domain on 20 September. The high AOT on 22 September corresponds with the Saharan dust layer around 2–4 km, inferred by the HALO aerosol type product, which utilizes spectral dependence of depolarization as well as lidar ratio (Burton et al. 2012), as well as by the aerosol backscatter coefficients above 10 Mm^{-1} sr^{-1}. The dust layer was transported by the flow associated with the strong coastal AEW trough. To document the impact of this dust outbreak on the thermodynamic conditions relevant to the MCSs near the coastline, the remaining discussion focuses on the flight path moving from the offshore region toward the coastline around 11°–12°N on both flights (highlighted in Figs. 5a,e).

Skew T diagrams show that the dust layer was associated with a strong inversion layer in the lower troposphere and dry midtroposphere on 22 September (Figs. 5f,g). Temperature increases and dewpoint temperature decreases sharply above

Unauthenticated | Downloaded 10/23/26 03:43 PM UTC

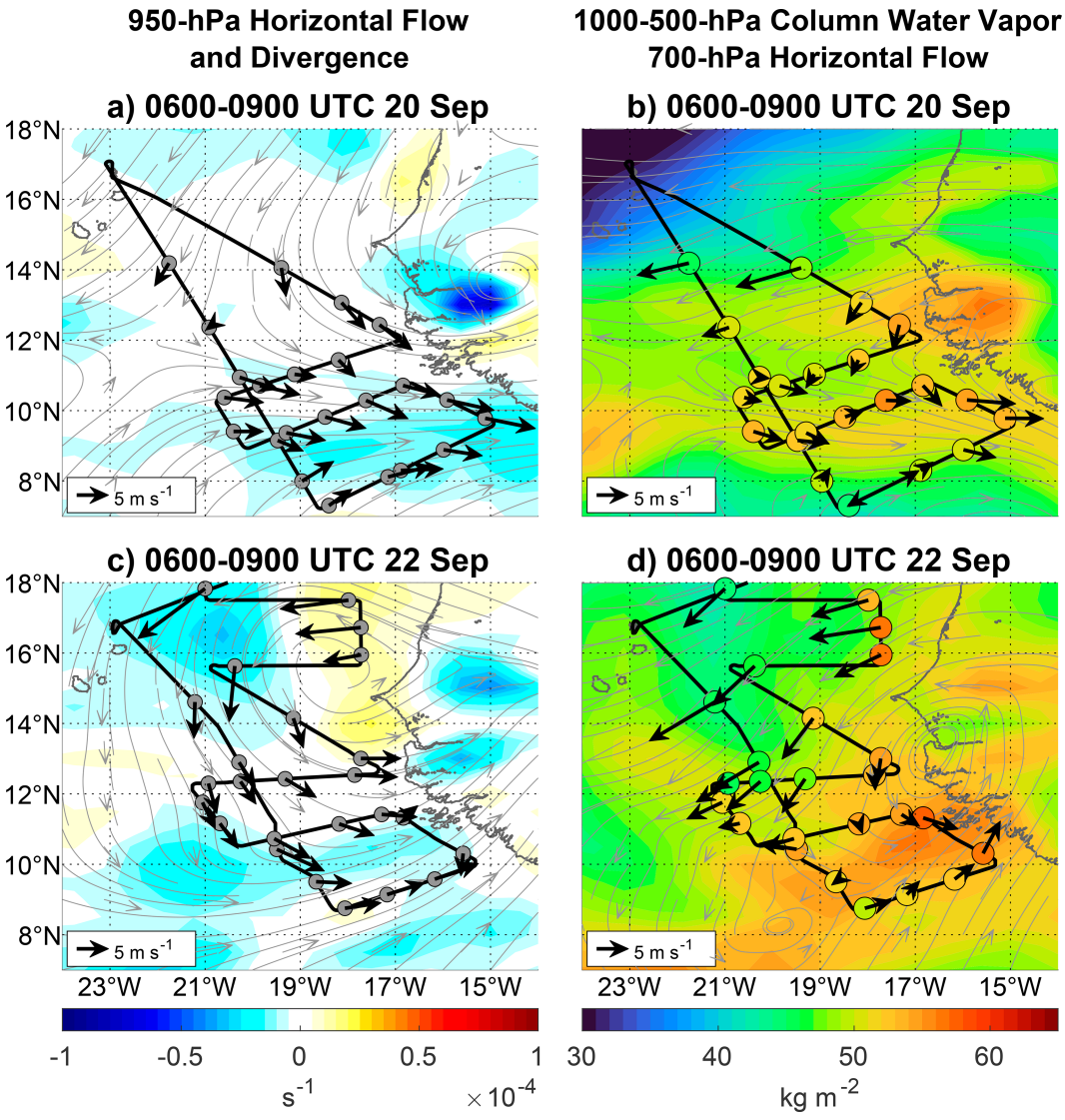


FIG. 3. Synoptic condition around the times of RF based on MERRA-2 and dropsonde data: (a),(b) RF 8 (0600–0900 UTC 20 Sep 2022) and (c),(d) RF 9 (0600–0900 UTC 22 Sep 2022). (left) MERRA-2 950-hPa horizontal winds (gray vectors), streamlines (gray lines), horizontal divergence (shaded; s^{-1}), and dropsonde 950-hPa horizontal winds (black vectors). (right) MERRA-2 and dropsonde 1000–500-hPa integrated column water vapor (shaded; kg), 700-hPa horizontal winds (gray and black vectors for MERRA-2 and dropsondes, respectively), and streamlines (gray lines).

around 900 hPa, showing the correspondence between the inversion layer and the height of high aerosol optical thickness in Figs. 4f and 4g. Given the warm and moist boundary layer, the LFC is low (below 900 hPa level), and the inversion layer associated with the dust layer appears above the LFC, not contributing to the calculated CIN while still inhibiting deep convection. The inversion layer and associated CIN-negative buoyancy weaken closer to the coastline, perhaps allowing coastal convection to develop (Fig. 5h). In contrast, such an inversion layer is not apparent on 20 September (Figs. 5b–d). The Saharan air layer (SAL) likely inhibited offshore convection, but convection remained active near the coastline on 22 September where the environment remained moist (Fig. 3d). On 20 September, convection was less active than on 22 September despite the lack of SAL as an inhibiting factor. However, CAPE was higher on 22 September than on 20 September, which may have contributed to different convective activity.

The relationship between precipitation and column water vapor is well documented by numerous previous studies (e.g., Bretherton et al. 2004; Ahmed and Schumacher 2015; Schiro et al. 2020; Wolding et al. 2020; Chen et al. 2023). However, it does not explain the different MCS activity over the coastal water between 20 and 22 September. Column-integrated water vapor exceeds 55 kg m^{-2} near the coastline for both days. These values also correspond to above 80% column

Unauthenticated | Downloaded 10/23/26 03:43 PM UTC

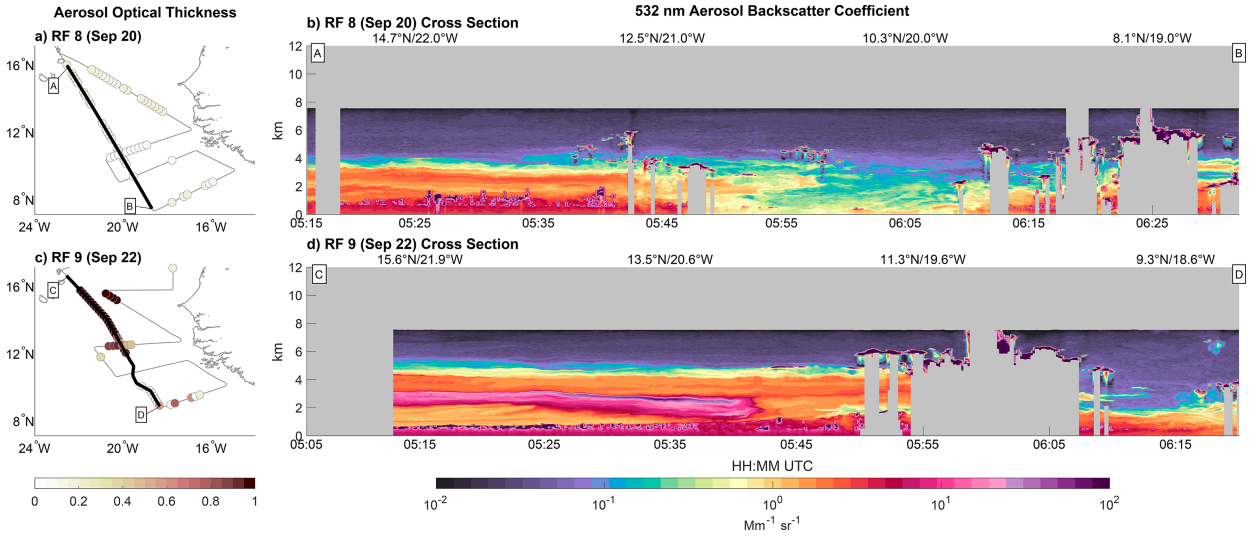


FIG. 4. (left) HALO AOT in the 0–5-km layer, obtained by integrating 532-nm aerosol extinction coefficients from (a) RF 8 (20 Sep) and (c) RF 9 (22 Sep). (right) Cross sections of HALO 532-nm aerosol backscatter coefficients along the highlighted track (thick black lines on the maps) from (b) RF 8 along points labeled A–B and (d) RF 9 along points C–D.

saturation fraction as defined by Bretherton et al. (2004), where precipitation increases exponentially above those values. Therefore, the column saturation of the coastal offshore was favorable for convective development on both days, yet MCSs remained small and short lived on 20 September.

While the column water vapor was similar, more water vapor was concentrated near the surface (below 1–2 km) on 22 September, while a deeper mixed layer appeared on 20 September (Fig. 6d). Some moist bias of HAMSR water vapor in 1–2 km is apparent compared to the dropsonde in Fig. 6, but all instruments (HAMSR, HALO, and dropsondes) consistently show a high concentration of water vapor near the surface on 22 September. The water vapor mixing ratio sharply decreases above 1–2 km, corresponding to the dust and associated inversion layer typically seen in the SAL profiles (Dunion 2011). The high water vapor concentration near the surface on 22 September may be due to suppressed vertical mixing by the inversion layer and/or increased surface latent heat flux.

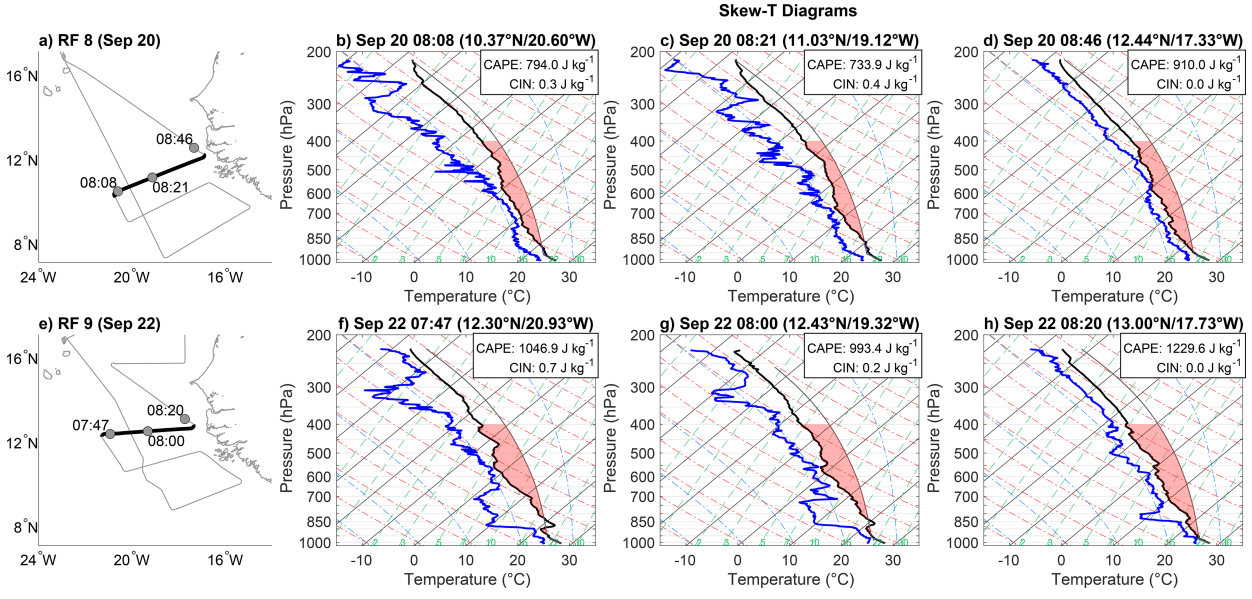


FIG. 5. Skew *T* diagrams of selected dropsonde data from (b)–(d) 20 Sep, RF8, and (g),(h) 22 Sep, RF9. (a),(e) The maps show the locations and times of the plotted dropsonde data. Black lines show temperatures, blue lines show dewpoint temperatures, and thin gray lines show parcel temperature with entrainment. The legends show the entraining CAPE and CIN below 400 hPa, corresponding to the red and blue shadings.

Unauthenticated | Downloaded 10/23/26 03:43 PM UTC

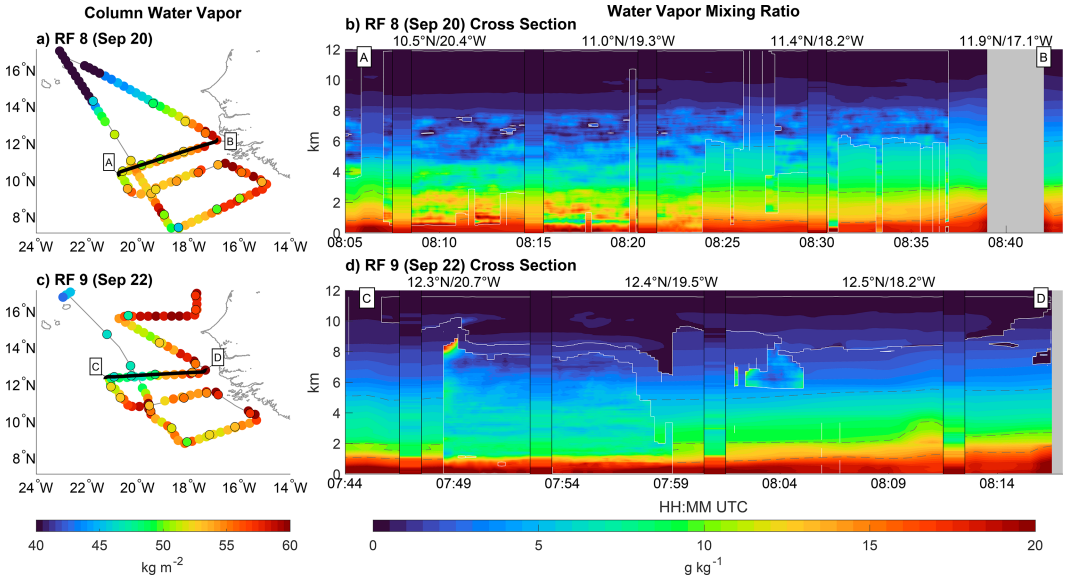


FIG. 6. (left) 500–1000-hPa integrated column water vapor from HAMSR (open circles) and dropsondes (outlined circles) on (a) 20 Sep, RF8, and (c) 22 Sep, RF9. (right) Vertical profiles of water vapor mixing ratio from HAMSR, HALO (outlined with white), and dropsondes (black outlined vertical columns) along the highlighted flight tracks (thick black lines on the left) from (b) RF 8 along points labeled A–B and (d) RF 9 along points C–D. HAMSR data were converted from pressure to altitude coordinates using the hydrostatic approximation. Black dashed lines contour at 5, 10, and 15 g kg^{-1} values of HAMSR.

This difference in the vertical distribution of water vapor persists even near the coastline (locations close to points B or D in Figs. 6b,d) despite the similar column-integrated water vapor between the 2 days. The near-surface higher water vapor on 22 September implies that the coastal marine boundary layer was close to saturation with small to no CIN and a low lifted condensation level (Fig. 5h), leading to high CAPE and requiring minimal mechanical forcing to initiate and sustain convection.

Another thermodynamic difference in the marine boundary layer between 20 and 22 September appears in equivalent potential temperature θ_e (Fig. 7). Average 0–1-km θ_e was several degrees higher on 22 than on 20 September north of 11°N, while it was lower in the south (around 10°N) on 22 than on

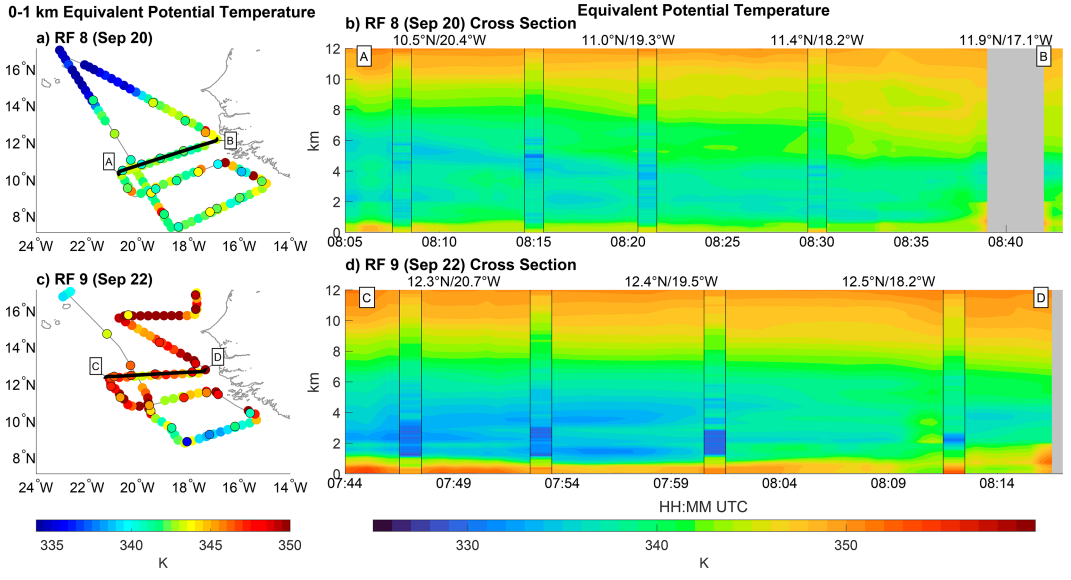


FIG. 7. As in Fig. 6, but showing 0–1-km average equivalent potential temperature on the left and its full vertical profiles on the right. Only HAMSR and dropsonde data are displayed.

Unauthenticated | Downloaded 10/23/26 03:43 PM UTC

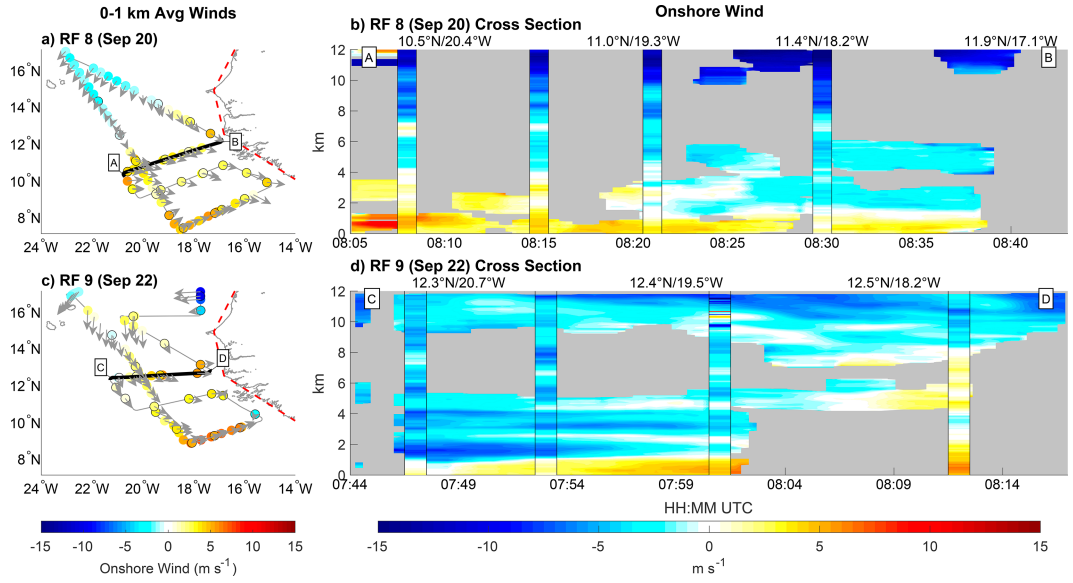


FIG. 8. As in Fig. 6, but showing (left) 0–1-km average DAWN and dropsonde horizontal winds in vectors and onshore winds in shading and (right) vertical profiles of onshore winds. Red dashed lines on the maps show the simplified coastline used to define onshore winds.

20 September. The higher θ_e north of 11°N on 22 September is likely due to the transport of warm Saharan air into the region and previously discussed effects of the inversion layer on trapping of moisture in the boundary layer. In addition, during the morning hours, the trapping of outgoing longwave radiation by dust probably has a net heating effect (Wong et al. 2009). Alternatively, sea surface temperature (SST) may be relevant, but daily SST near the coastline from NOAA OISST version 2 data (Huang et al. 2021) was warmer on 20 than on 22 September (not shown). Therefore, the significantly higher boundary layer θ_e on 22 than on 20 September is likely explained by the advection of warm Saharan air into the region and the impacts of the associated inversion layer. The higher boundary layer moisture and θ_e on 22 September may have supported the development of larger and longer-lasting MCSs by increasing entraining CAPE (Fig. 5).

The effects of different thermodynamic conditions on MCSs can also depend on the origin of air that flows into MCSs. As discussed in section 3, the nearby AEW trough on 22 September led to stronger near-surface onshore flow (Fig. 8c), while the flow was more northwesterly (parallel to the coastline) on 20 September without a nearby AEW (Fig. 8a). To quantify the difference in the onshore flow, we define onshore flow as the component of the horizontal winds directed to the closest simplified coastline (red dashed lines in the left column of Fig. 8).

Onshore flow is seen on both 20 and 22 September, but the spatial variability differs between the 2 days. On 20 September, the onshore flow became shallower and weaker toward the coastline (Fig. 8b). In contrast, on 22 September, the onshore flow became stronger and deeper toward the coastline (Fig. 8d). DeLonge and Fuentes (2012) also documented the relationship between stronger boundary layer onshore flow at the coastline with significant SAL events, analogous to the observed conditions on 22 September. The combined presence of strong onshore flow and high boundary layer θ_e on 22 September implies that the inflow air of the MCSs had higher θ_e than on 20 September, potentially supporting MCS development and growth. At the same time, the coastal surface drag and orography effects may have enhanced surface convergence around the coastline on 22 September, providing a stronger mechanical forcing as well. This latter mechanism cannot be assessed with our observational datasets.

b. *Environmental relationship with coastal MCSs from a storm-relative perspective*

The different synoptic conditions of 20 and 22 September suggest that the strength and thermodynamic properties of boundary layer inflow air may have influenced the MCS development. This section reexamines the relationship between MCS properties and MCS-relative environments. We focus this analysis only on dropsonde data as retrievals of HALO and DAWN are limited in the immediate environment of MCSs due to increased cloudiness. While HAMSR data are available in precipitating areas, previous analyses revealed moist and warm biases of HAMSR retrievals in precipitating areas (e.g., Figs. 6 and 7). Dropsondes do not have these issues, while their number is limited. Another limitation is that the observations do not fully cover the continuous three-dimensional environment around each MCS. Therefore, the compared airborne measurements around MCSs are never truly equivalent. These typical caveats in the analysis of airborne data are reduced by comparing the two flights that took similar flight paths on 20 and 22 September. Still, these caveats should be considered in the interpretations.

Unauthenticated | Downloaded 10/23/26 03:43 PM UTC

We first examine the relationship between the column-integrated water vapor near MCSs and their rain rates and sizes. The column-integrated (1000–500 hPa) water vapor is taken only within the "prestorm environment," defined as ±90° from the direction of MCS motion and within 150 km from the edges of contiguous raining grids defined as the MCS by TIMPS tracks. We estimate MCS motion based on TIMPS tacks after smoothing the tracks with a 2-h moving smoothing window with triangular weights, removing unphysical abrupt changes in TIMPS tracks caused by its discrete (30-min) data. We only take the prestorm environment to eliminate the environment perturbed by the MCSs. The MCSs on 20 and 22 September were slowly moving away from the coastline, so most of the data collected over coastal waters were identified as being in the pre-MCS environment. The quantification of column water vapor in the prestorm environment is done for all MCSs (MCS1–MCS4) on 20 and 22 September and compared with 30-min MCS rain rates and sizes from TIMPS at times closest to the times of environment sampling.

Figures 9a and 9b show that column water vapor in the environment does not clearly distinguish the rain rates or size of the MCSs on 20 and 22 September (as shown in Fig. 6). While the column water vapor was relatively high around coastal MCSs on both days (around 50–60 kg m^{-2}), MCS mean rain rates ranged from 2 to 6 mm h^{-1}, and MCS sizes ranged widely (10^3–10^5 km^2). Therefore, the amount of column water vapor does not explain the different coastal MCS properties between 20 and 22 September.

Another difference on 20 and 22 September was the strength of the onshore flow (Fig. 8), which relates to the strength of the MCS inflow that has been linked to the width of updrafts (Peters et al. 2022b). To find the strength of inflow air, we first define storm-relative horizontal winds as the difference between observed horizontal winds and the smoothed MCS motion. After removing the MCS motion, we find storm-relative inflow as the component of the storm-relative horizontal winds directed toward the MCS center (TIMPS track location). The storm-relative inflow typically appeared within 0–2 km altitudes, the layer over which the storm-relative inflow is averaged to define the boundary layer storm-relative inflow. Whenever this storm-relative inflow is positive, it is identified as the boundary layer inflow layer, and we find its magnitude.

The boundary layer storm-relative inflow ranges from near zero to 10 m s^{-1}, with the strongest inflow around MCS3 on 22 September (Figs. 9c,d). This difference relates to the stronger near-surface onshore flow observed on 22 September (Fig. 8). However, the strength of inflow does not seem to distinguish MCS properties, as a wide range of MCS mean rain rates and sizes can be found with similar inflow strengths. Given the strength of inflow may relate to the strength of vertical wind shear, we also examined the vertical wind shear of inflow winds in the boundary layer (0–2 km) and lower free troposphere (2–5 km) in the prestorm environment. However, we did not find any clear relationships between the vertical wind shear and MCS properties (not shown).

While the inflow strength does not distinguish MCS properties, the thermodynamic properties of the inflow air relate to the MCS properties. To check their relationship with MCS properties, we find the average water vapor mixing ratio and equivalent potential temperature in the identified inflow layers. MCS rain rates and sizes tend to increase with increasing equivalent potential temperature in the inflow air, with a few exceptions for MCS3 on 22 September (dots marked with "S" in Figs. 9e–h). MCS3 had a few observations of inflow air with low equivalent potential temperature (337–339 K), which occurred on the south side of the MCS at around 10°N. On 22 September, the boundary layer equivalent potential temperature decreased toward the equator, with particularly low values around 10°N (Fig. 7). This lower equivalent potential temperature southward might be why MCS3 eventually dissipated and a new MCS4 developed to its north on 22 September. With these exceptions, MCS mean rain rates and sizes strongly relate to the equivalent potential temperature in the boundary layer inflow air. Similar relationships appear with the boundary layer water vapor mixing ratio, implying its dominant contribution to the variability in equivalent potential temperature.

The above analysis of the relationship between MCS properties and the environment over coastal waters from dropsondes provides evidence for the potential importance of boundary layer thermodynamic properties in inflow air. On both 20 and 22 September, the high amount of column water vapor was favorable for MCS development over the coastal waters. However, the significant difference between the 2 days appears in the boundary layer thermodynamic and kinematic properties, which are likely caused by AEW influences. The high equivalent potential temperature of inflow air may increase the buoyancy due to the lower lifting condensation level and reduced drying effects of entrainment (Emanuel et al. 1994; Kingsmill and Houze 1999; Schiro et al. 2020). This is supported by Figs. 9i and 9j, which show that the coastal MCSs on 22 September tend to have higher entraining CAPE in their inflow air than on 20 September. Therefore, while the limited airborne observations do not allow us to firmly conclude which factor is most relevant to MCS properties, the modulation of boundary layer properties by AEWs appears important to understanding what modulates MCS properties over the West African coastal waters. The following section examines the applicability of this conclusion from the two cases on 20 and 22 September to historical data.

5. Historical relationships between AEW and MCSs over coastal water

The comparison of 20 and 22 September during CPEX-CV suggests the strong influence of AEW on coastal MCSs by modulating the environment. In particular, MCS was more active over the coastal water when the strong AEW trough was near the coastline on 22 September. This active MCS was related to enhanced near-surface onshore flow, convergence, boundary layer moisture, and equivalent potential temperature. This section demonstrates that these modulations of environment and MCSs by AEWs also appear using historical data from June to September 2011–21. The statistical significance of all results in this section is tested using 1000 iterations of bootstrap resampling.

Unauthenticated | Downloaded 10/23/26 03:43 PM UTC

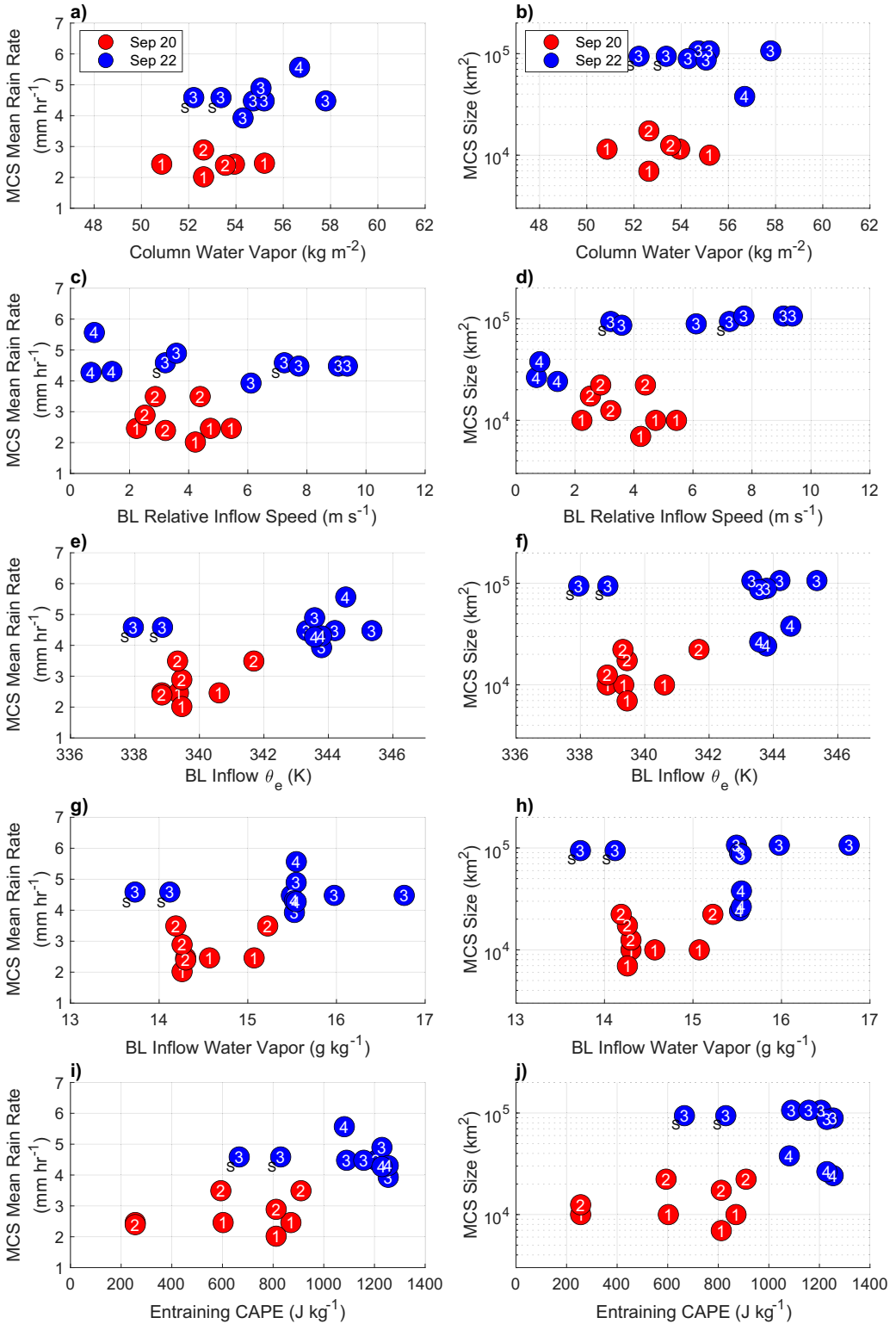


FIG. 9. Scatterplots of MCS (left) mean rain rates and (right) sizes with dropsonde environment variables within 150 km of the MCSs. From top to bottom, each row shows (a),(b) surface-to-500-hPa column-integrated water vapor, (c),(d) 0–2-km relative inflow speed, (e),(f) 0–2-km equivalent potential temperature of inflow air, (g),(h) 0–2-km water vapor mixing ratio of inflow air, and (i),(j) entraining CAPE up to 400 hPa of inflow air. Red and blue dots show the 20 and 22 Sep observations, respectively. Numbers within dots show the corresponding MCS numbers in Fig. 1. The dots with S on their bottom-left corner indicate points collected south of 10°N on 22 Sep.

Unauthenticated | Downloaded 10/23/26 03:43 PM UTC

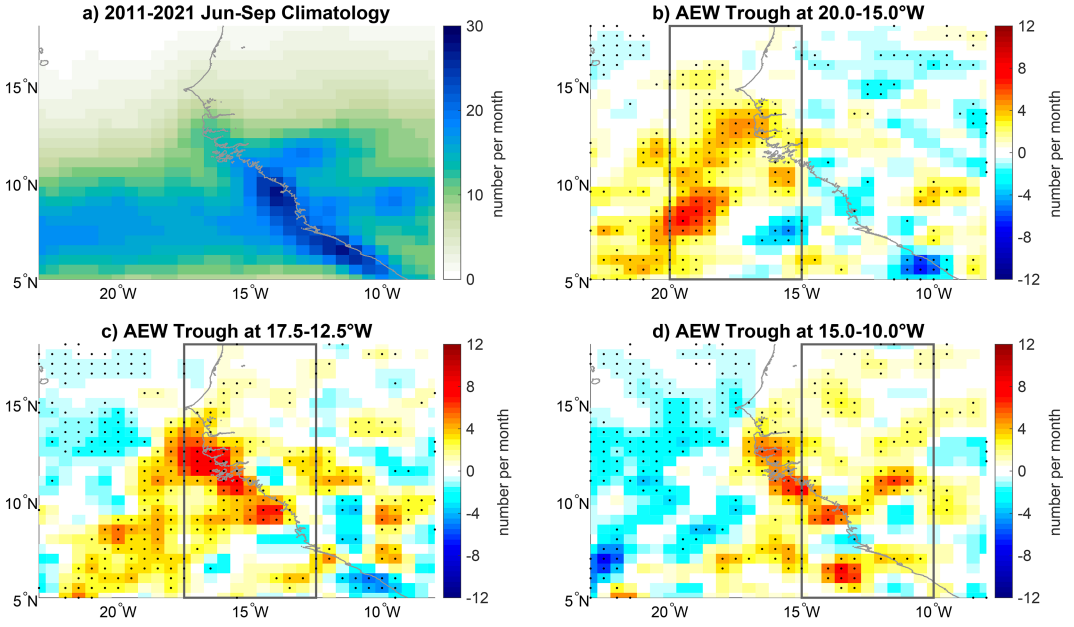


FIG. 10. (a) June–September 2011–21 climatological frequency of MCS tracks (number per 30-day month). Anomalous frequency of MCS tracks when the AEW trough is at (b) 20°–15°W, (c) 17.5°–12.5°W, and (d) 15°–10°W within 5°–20°N latitudes. Black dots show statistically significant anomalies at the 95% confidence level.

a. Modulation of coastal MCS frequency and properties

The climatological frequency of MCSs during June–September shows that MCS occurrence is most frequent near the coastline, especially along 5°–10°N (Fig. 10a). About 30 MCSs occur per month near the coastline, implying a nearly daily presence of MCSs. The high frequency of MCS over the coastal region is partly attributed to the presence of the Guinea Highlands that enhance MCS, AEW, and their coupling through their effect on temperature distribution and flow blockage (Tompkins and Chiao 2012; Hamilton et al. 2017, 2020; Wu et al. 2024).

Our analysis shows that MCSs around the coastline occur more frequently within and slightly west of AEW troughs (Figs. 10b–d), agreeing with some of the prior studies (Dieng et al. 2014; Janiga and Thorncroft 2016). The changes in the frequency of coastal MCSs with AEWs also appear stronger over the coastal ocean than over land and poleward of 7.5°N than equatorward of this latitude. This result implies that AEW modulation of MCS frequency is stronger north of the average ITCZ latitude than within the ITCZ.

Figures 11a and 11b also demonstrate the latitude-dependent relationships between AEW and coastal MCSs. These figures show the relative longitude distributions of AEW troughs from the MCS longitudes at the times of MCS occurrence within 200 km of the coastline on either land or ocean sides. The distributions are found for coastal MCSs at different latitudes. Such distributions of relative AEW locations are normalized by subtracting and dividing by the climatological distributions of AEW troughs around the coastline at the corresponding latitude bins. Given that we use the relative locations of AEWs from the varying locations of coastal MCSs, the typical climatology of AEW troughs on fixed geographical grids is inappropriate to normalize the distribution. Therefore, the climatological distribution of AEW troughs is found by finding relative longitudes of AEWs from observed coastal MCS locations but on randomly selected dates (instead of the true observed times of MCSs). This process is iterated 1000 times, and their average gives the climatological distribution of relative AEW longitudes, while the spread gives the confidence level. The comparison to such climatological distribution tests the null hypothesis that the relative AEW distribution on the specific dates of observed coastal MCSs is indistinguishable from the distribution that would result from selecting random dates.

MCS occurrence over coastal land and ocean coincides with increased occurrence of nearby AEW troughs (Figs. 11a,b). However, the relationship strength between the MCSs and AEWs depends on the latitudes and whether the MCSs are over the coastal land or ocean. The coastal AEW troughs significantly enhance MCS occurrence over coastal land exclusively poleward of 12.5°N, while they enhance MCS occurrence over the coastal ocean at all latitudes between 5° and 15°N. Both MCSs over coastal land and ocean occur most frequently when AEW troughs are located a few degrees east of them. These results imply that coastal land and ocean MCSs tend to occur slightly ahead of AEW troughs, but such AEW impacts are stronger for coastal ocean than land MCSs and ones that occur farther north than closer to the equator.

MCS occurrence also weakly coincides with the increased existence of AEW troughs at about 16°–18° west or east of coastal MCSs (Figs. 11a,b) due to the expected concurrent occurrence of AEW troughs separated by their typical zonal wavelength of 2000–4000 km (Kiladis et al. 2006). However, among the dates when an AEW trough is approximately 20° offshore from the

Unauthenticated | Downloaded 10/23/26 03:43 PM UTC

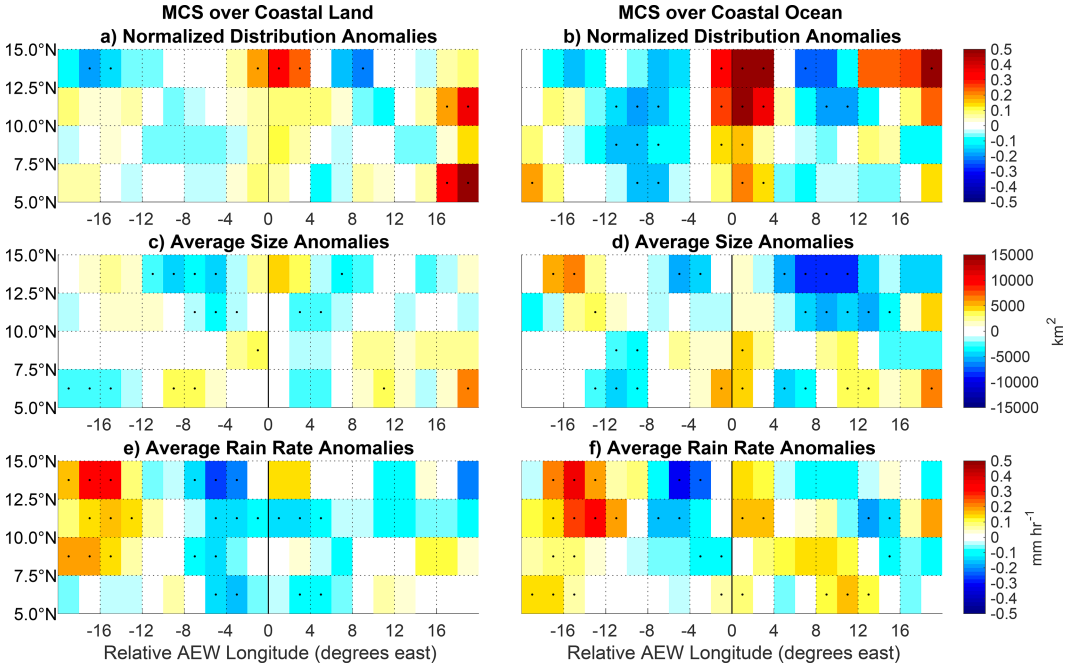


FIG. 11. (a),(b) Normalized distribution anomalies of AEW trough's longitudes relative to MCS longitude over coastal land and ocean between 5° and 15°N. Coastal land and ocean are defined as within 200 km from the nearest western coastline of West Africa. Positive and negative relative AEW longitudes indicate that the position of AEW trough is east and west, respectively, of MCS longitude. (c),(d) Mean anomalous size and (e),(f) mean anomalous rain rates of MCSs, conditioned by the relative longitudes of AEW troughs and latitudes of MCSs.

coastline (around 35°W), only a small fraction (about 5%–10%) of those dates have another AEW trough near the coastline. Therefore, stronger anomalies of MCS frequency with AEW troughs near the coastline as opposed to farther offshore suggest that the coastal AEW troughs are likely influencing MCS occurrence instead of remote AEW troughs farther offshore.

In addition to the frequency of coastal MCSs, the relative location of AEWs influences the size and mean rain rate of coastal MCSs (Figs. 11c–f). When the coastal land MCSs occur with an AEW trough at about 0°–4° eastward (inland) of MCSs, MCS sizes tend to be anomalously larger at 12.5°–15°N, but these anomalies are not statistically significant. MCSs over coastal water also show a significant increase in size at lower latitudes (around 5°–10°N) when AEW troughs are nearby. The average rain rates of coastal MCSs are also anomalously higher when AEW troughs are about 0°–4° eastward of the MCSs. However, this relationship between MCS rain rates and AEW troughs only appears weakly for MCSs poleward of 10° or 12.5°N over coastal ocean and land, respectively. The weakly enhanced MCS rain rates and sizes with nearby AEW troughs might be partly due to the increased frequency and/or lifetime of MCSs, which increases the chance that MCSs can grow and develop more intense rain rates.

Rather than when AEW troughs are near the coastline, the average rain rates of coastal MCSs are significantly higher when AEW troughs appear about 12°–18° west of MCSs. The effects of such offshore AEW troughs are seen in MCS sizes, exclusively over coastal oceans poleward of 12.5°N. Therefore, when AEW troughs are farther offshore, they tend to generate coastal MCSs with higher rain rates that may grow into anomalously large MCSs over coastal waters. These results imply that the AEWs modulate MCS rainfall intensity and size differently than MCS frequency. Coastal MCSs become most frequent when AEW troughs are close to the coastline, but their rainfall intensity and sizes increase when AEW troughs are farther offshore, about 12°–20° west.

The 20 and 22 September comparison during CPEX-CV (2022) matches the historical statistics of relationships between coastal MCSs and AEWs. A strong AEW trough was near the coastline on 22 September, while it was absent or weak on 20 September. Consistent with the historical statistics, MCSs persisted near the coastline on 22 September (which is tied to increased frequency) than on 20 September without a strong AEW trough. The consistency of case studies from CPEX-CV with historical statistics suggests that the compared atmospheric conditions on 20 and 22 September in section 4 may represent how AEWs typically modulate coastal environments.

b. *Modulation of the coastal environment*

To examine the analogy between the historical AEW modulation of the coastal environment and CPEX-CV cases, we composite anomalous kinematic and thermodynamic fields using MERRA-2 conditioned by the longitudes of AEW troughs. We focus on the times when AEW troughs are near the coastline and about 15° west of the coastline. These two locations represent times when coastal MCSs become most frequent versus when they have higher rain rates and larger sizes (Fig. 11). The coastal location of the AEW trough is analogous to the synoptic

Unauthenticated | Downloaded 10/23/26 03:43 PM UTC

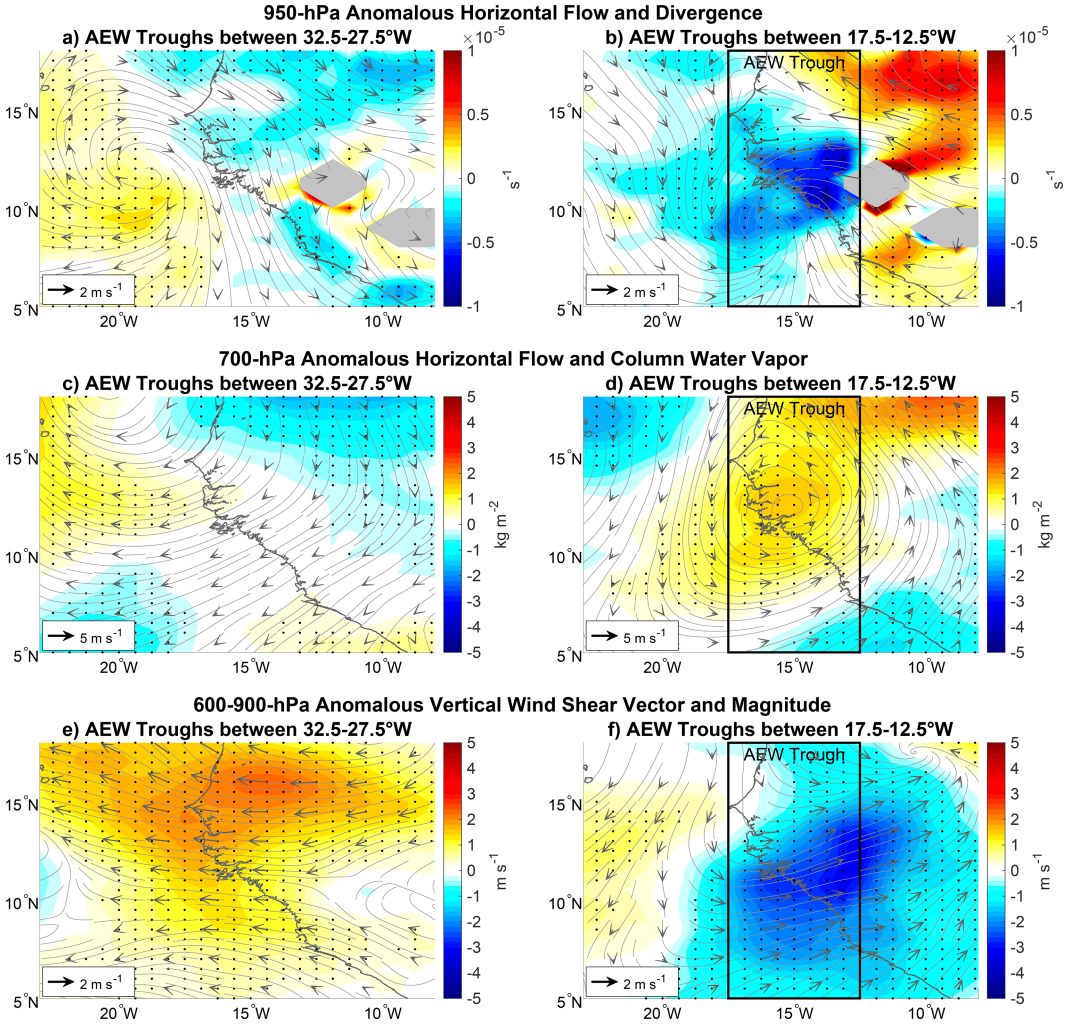


FIG. 12. Composite maps of anomalous (a),(b) 950-hPa horizontal divergence (shaded; s^{-1}), winds (vectors), and their streamlines; (c),(d) surface-to-500-hPa column-integrated water vapor (shaded; g kg^{-1}), 700-hPa winds, and streamlines; and (e),(f) magnitudes, vectors, and streamlines of 600–900-hPa vertical difference in horizontal winds (m s^{-1}). Dots indicate statistically significant anomalies of shaded quantities at 95% confidence level. All plotted vectors are statistically significant at the same confidence level.

condition shown on 22 September of CPEX-CV. All composites are done at 0300–0900 UTC to facilitate the comparison with the 22 September case, when all airborne data were collected in the early to midmorning. All anomalies in this section represent deviations from the averages over the analyzed period (June–September 2011–21).

When AEW troughs are near the coastline, coastal regions have anomalous cyclonic circulation and enhanced near-surface convergence (Fig. 12b). The area of anomalous convergence appears north of the typical ITCZ latitude, which was also seen on 22 September of CPEX-CV (Fig. 3b). The enhanced convergence appears over both coastal land and ocean. The convergence is stronger over land in MERRA-2, which may be due to the presence of the Guinea Highlands (Zuluaga and Houze 2015; Hamilton et al. 2017), but the convergence is strongest over coastal waters using ERA5 (not shown). Regardless of some uncertainty in the precise pattern of surface convergence in reanalyses, the coastal surface convergence is associated with anomalous deep rising motion, seen from the longitude–pressure cross section at 12.5°–15°N (Fig. 13b). The average surface winds from the historical period do not show enhanced onshore (westerly) flow at the same latitudes as observed on 22 September of CPEX-CV (Fig. 13f), but the enhanced surface convergence around the coastline implies enhanced mechanical lifting and near-surface inflow to coastal MCSs.

Column-integrated water vapor also increases around the coastline when the AEW trough is near the coastline (Fig. 12d). The entire vertical column of air near the coastline has anomalously high specific humidity, which closely relates to anomalous equivalent potential temperature (Fig. 13d). The enhanced specific humidity and equivalent potential temperature also appear

Unauthenticated | Downloaded 10/23/26 03:43 PM UTC

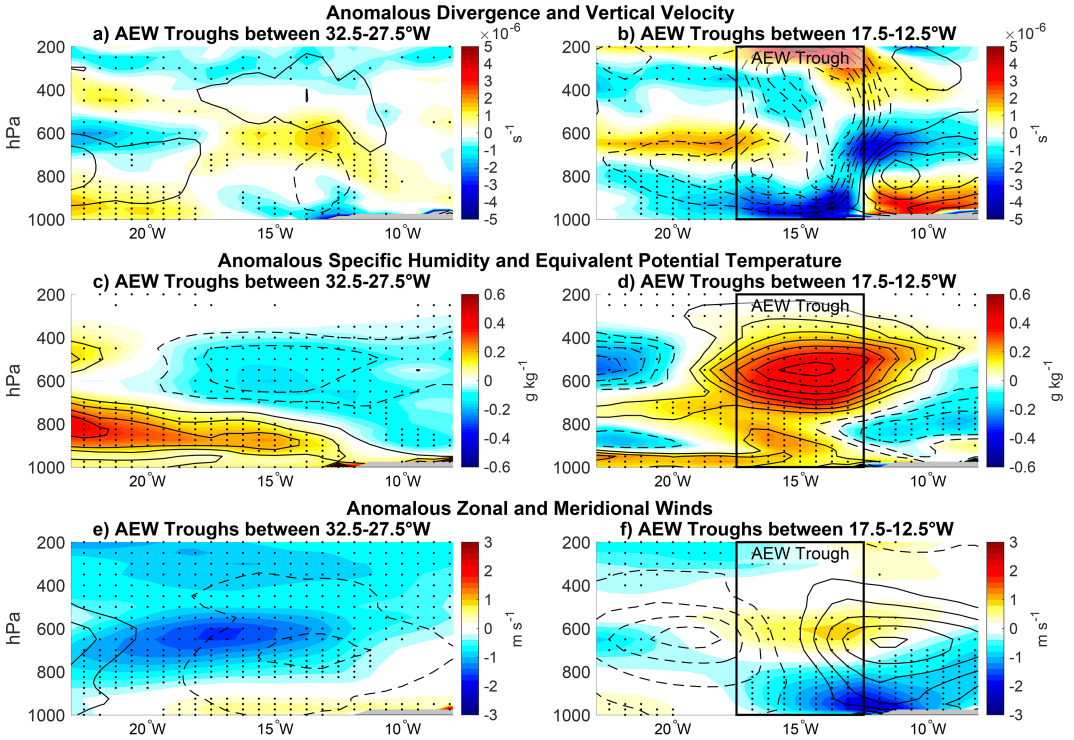


FIG. 13. Longitude–pressure cross sections of anomalous (a),(b) divergence (shaded; s^{-1}) and vertical pressure velocity (contoured every 0.02 Pa s^{-1} interval), (c),(d) specific humidity (shaded; g kg^{-1}) and equivalent potential temperature (contoured every 0.2-K interval), and (e),(f) zonal (shaded; m s^{-1}) and meridional winds (contoured every 0.5 m s^{-1}) at 0300–0900 UTC. Solid contours indicate positive and dashed contours indicate negative values. The composites when AEW troughs are identified (left) between 32.5° and 27.5°W and (right) between 17.5° and 12.5°W.

near the surface (below 900 hPa), which zonally extends offshore from the coastal area. This enhanced boundary layer humidity and equivalent potential temperature were similarly observed on 22 September of CPEX-CV (Figs. 6, 7). Therefore, the reanalysis data also suggest that the equivalent potential temperature of boundary layer inflow air is typically higher for coastal MCSs when the AEW trough is nearby. At the same time, the typically higher column humidity around AEW troughs supports MCS development, while no substantial difference in column humidity was seen around the coastline between 20 and 22 September of CPEX-CV.

These results indicate that the reanalysis also shows similar perturbation of the coastal environment by AEWs as observed on 22 September of CPEX-CV. The surface convergence zone is shifted northward from the ITCZ latitude and is enhanced around the coastline, providing mechanical lifting. At the same time, enhanced water vapor over the tropospheric column and in the boundary layer apparently supports deep convection development. We hypothesize that the mechanical forcing and high humidity support deep convection development and MCS formation by helping form relatively wide updraft cores, which are less susceptible to dilution of buoyancy by entrainment, and reducing entrainment of dry air (Holloway and Neelin 2009; Morrison et al. 2022; Galarneau et al. 2023; Chen et al. 2023; Powell 2024). Previous studies have found that the AEW and convection interact differently over land and ocean, where adiabatic forcing of vertical motion is more relevant over land, while moisture is more relevant over ocean (Kiladis et al. 2005; Janiga and Thorncroft 2016). These two separate mechanisms may be occurring together, uniquely over the coastal region.

In contrast, when AEW troughs are farther offshore, surface convergence and column-integrated water vapor are close to neutral near the coastline (Figs. 12a,c). Instead, the AEW troughs farther offshore enhance the African easterly jet (AEJ) and associated vertical wind shear below the jet (Figs. 12e, 13e). While vertical wind shear can suppress deep convection by increasing entrainment and generating downward dynamical pressure gradient force (Peters et al. 2019), the shear can also help organize convection (Robe and Emanuel 2001; Cheng et al. 2020). Vertical wind shear can enhance deep convective initiation when initial updrafts exceed a certain width, while narrower initial updrafts will be suppressed by the shear (Peters et al. 2022a,b; Maybee et al. 2024). These previous results may explain why fewer but more intense MCSs form near the West African coastline when AEWs induce strong vertical wind shear. Under the strong vertical wind shear, fewer, sufficiently wide, initial updrafts may develop into deep convection, but those can then develop into large MCSs with intense rain rates.

An AEW trough was offshore on 20 September (around 28°–30°W; Fig. 2b). However, this date did not represent the

Unauthenticated | Downloaded 10/23/26 03:43 PM UTC

condition when more intense MCSs form. This AEW trough on 20 September was relatively weak (curvature vorticity of about 1×10^{-5} s^{-1}) and located south (8°–9°N) of typical AEW latitudes (around 15°N). Therefore, neither the AEJ nor vertical wind shear was particularly strong (Fig. 3a), which is likely why this offshore AEW did not influence coastal MCSs as expected from typical offshore AEWs.

6. Conclusions

This study compares the observed atmospheric environment surrounding MCSs over the western coastal waters of West Africa between 20 and 22 September 2022, when synoptic conditions and MCS activity were different. On these two dates, the NASA CPEX-CV field campaign collected high-resolution airborne kinematic and thermodynamic data over the coastal marine environment, where observations are limited. Climatologically, MCSs are frequently seen in this coastal monsoon environment as MCSs frequently form over the coastal water and land, which then propagate offshore (Wu et al. 2024). However, the two analyzed days provide case studies demonstrating that synoptic variability, dominated by AEWs over this region, strongly influences the coastal marine environment and MCS properties. We document the key observed differences in the coastal marine environment between these dates to understand the mechanisms influencing MCSs at this land-to-ocean transition zone. We also use satellite and reanalysis data to validate the representation of the limited CPEX-CV case studies for a larger sample size of typical AEW–coastal MCS relationships.

One of the key differences between 20 and 22 September 2022 is the lack and presence of a strong AEW trough near the coastline, which modulated kinematic and thermodynamic conditions for MCS development. On 20 September, MCSs appeared around the 10°–14°N coastline, but they were small and short lived when no AEW troughs were nearby or an AEW-like trough was nearby but too weak to substantially modify the environment. In contrast, on 22 September, large and long-lived MCSs stalled at similar locations when a strong AEW trough was near the coastline. The coastal AEW trough on 22 September led to stronger near-surface monsoon onshore flow and shifted the surface convergence zone northward from the typical ITCZ latitude, providing stronger mechanical lifting in the coastal regions of MCS development. The AEW on 22 September also contributed to the offshore transport of the dusty, dry, and warm SAL layer, generating an inversion layer offshore, while the coastal waters remained moist around the AEW trough. While the lower free troposphere was dry due to the SAL layer, below the dry SAL layer, the suppression of mixing by the inversion layer and the warm SAL layer offshore likely created the warm and moist boundary layer, representing about 7–10-K higher boundary layer equivalent potential temperature on 22 September than on 20 September. Then, the strengthened surface monsoon onshore flow led to a stronger inflow of higher equivalent potential temperature to the coastal MCSs on 22 September, likely sustaining MCS development.

The historical 11 years of monsoon season analysis also indicates that coastal MCSs are most frequent when AEW troughs approach the coastline. The high frequency of coastal MCSs implies that they form more frequently and/or sustain longer, which increases the chance of seeing larger and more intense MCSs. Therefore, 22 September 2022 likely represents how AEW and coastal MCSs typically interact. While there is uncertainty in the accuracy of reanalysis, particularly in the boundary layer (Wolding et al. 2022), MERRA-2 also captures similar kinematic and thermodynamic perturbations of coastal water by AEWs as seen on 22 September.

While coastal MCSs become more frequent with a nearby AEW trough, the historical analysis also revealed that MCSs with anomalously high rain rates are more likely to occur when AEW troughs are farther offshore (about 12°–20° west of the coastline). At such AEW positions, the AEJ and associated vertical wind shear are significantly enhanced around the coastline. The strong vertical wind shear does not enhance the number of MCSs. However, the ones that form develop more intense rain rates, which supports the idea that vertical wind shear can help organize convection (Robe and Emanuel 2001; Cheng et al. 2020) and conditionally support deep convection when the updrafts meet the appropriate conditions for growth (Peters et al. 2022a). How the occurrence of such coastal MCSs with more intense rain rates influences or interacts with subsequent AEW troughs may be considered in a future study.

These results aid the understanding of how AEWs and MCSs interact around the coastline, the transition zone between land and ocean where their interactions were known to differ (Janiga and Thorncroft 2016; Schwendike and Jones 2010). Coastal monsoon regions, such as the western coast of West Africa, are important to the global hydrological cycle given their high rainfall, but their unique rainfall and convective properties remain challenging to simulate (Kouadio et al. 2020; Tao et al. 2023). Our study demonstrates that synoptic variability can strongly perturb the environment and influence MCS frequency and properties over the coastal regions in a manner different from inland or open ocean. Therefore, capturing the synoptic variability of coastal MCSs is important to obtain an accurate climatological average and spread of MCS activity. Further studies on how synoptic conditions influence the convective structures of MCSs and land–ocean–atmosphere interactions would aid the understanding of coastal MCS processes and their potential feedback onto AEWs.

Acknowledgments. We acknowledge the support of this work by Grant 80NCCS20K0901 of the NASA Weather and Atmospheric Dynamics Program. We also thank the efforts of all team members of the NASA CPEX-CV, who contributed to the collection of data used in this study. R. R.-B. acknowledges that part of this material was based on work supported by the National Center for Atmospheric Research, a major facility sponsored by the U.S. National Science Foundation under Cooperative Agreement 1852977. Part of this work was carried out at the Jet Propulsion Laboratory, California Institute of Technology, under contract

Unauthenticated | Downloaded 10/23/26 03:43 PM UTC

to NASA (80NM0018D0004). We thank the three anonymous reviewers for feedback to improve the manuscript.

Data availability statement. All data collected through the NASA CPEX-AW are available from https://asdc.larc.nasa.gov/project/CPEX-CV (Nowottnick et al. 2024). TIMPS tracking data are available from https://home.chpc.utah.edu/~mani/TIMPS_v2/ (Rajagopal et al. 2023). MERRA-2 reanalysis data are available from https://disc.gsfc.nasa.gov/datasets?project=MERRA-2 (Gelaro et al. 2017). The codes used to calculate the two versions of the AEW tracking data used in this study are available from https://doi.org/10.5281/zenodo.10076723 (mahollis3313 2023) and https://github.com/qlawton/QTrack (Lawton et al. 2022).

REFERENCES

Ahmed, F., and C. Schumacher, 2015: Convective and stratiform components of the precipitation-moisture relationship. *Geophys. Res. Lett.*, **42**, 10 453–10 462, https://doi.org/10.1002/2015GL066957.

Bedka, K. M., and Coauthors, 2021: Airborne lidar observations of wind, water vapor, and aerosol profiles during the NASA Aeolus calibration and validation (Cal/Val) test flight campaign. *Atmos. Meas. Tech.*, **14**, 4305–4334, https://doi.org/10.5194/amt-14-4305-2021.

Bercos-Hickey, E., T. R. Nathan, and S.-H. Chen, 2020: On the relationship between the African easterly jet, Saharan mineral dust aerosols, and West African precipitation. *J. Climate*, **33**, 3533–3546, https://doi.org/10.1175/JCLI-D-18-0661.1.

Berry, G. J., and C. Thorncroft, 2005: Case study of an intense African easterly wave. *Mon. Wea. Rev.*, **133**, 752–766, https://doi.org/10.1175/MWR2884.1.

Biasutti, M., S. E. Yuter, C. D. Burleyson, and A. H. Sobel, 2012: Very high resolution rainfall patterns measured by TRMM precipitation radar: Seasonal and diurnal cycles. *Climate Dyn.*, **39**, 239–258, https://doi.org/10.1007/s00382-011-1146-6.

Borne, M., P. Knippertz, M. Weissmann, B. Witschas, C. Flamant, R. Rios-Berrios, and P. Veals, 2024: Validation of Aeolus L2B products over the tropical Atlantic using radiosondes. *Atmos. Meas. Tech.*, **17**, 561–581, https://doi.org/10.5194/amt-17-561-2024.

Bretherton, C. S., J. R. McCaa, and H. Grenier, 2004: A new parameterization for shallow cumulus convection and its application to marine subtropical cloud-topped boundary layers. Part I: Description and 1D results. *Mon. Wea. Rev.*, **132**, 864–882, https://doi.org/10.1175/1520-0493(2004)132<0864:ANPFSC>2.0.CO;2.

Brown, S. T., B. Lambrigtsen, R. F. Denning, T. Gaier, P. Kangaslahti, B. H. Lim, J. M. Tanabe, and A. B. Tanner, 2011: The high-altitude MMIC sounding radiometer for the global hawk unmanned aerial vehicle: Instrument description and performance. *IEEE Trans. Geosci. Remote Sens.*, **49**, 3291–3301, https://doi.org/10.1109/TGRS.2011.2125973.

Burgess, R. W., and M. I. Oyola-Merced, 2024: Saharan dust impact on radiative heating rate errors inherent in reanalysis data in the African easterly wave development region. *Atmos. Chem. Phys.*, **24**, 12 183–12 201, https://doi.org/10.5194/acp-24-12183-2024.

Burton, S. P., and Coauthors, 2012: Aerosol classification using airborne high spectral resolution lidar measurements—Methodology and examples. *Atmos. Meas. Tech.*, **5**, 73–98, https://doi.org/10.5194/amt-5-73-2012.

Carroll, B. J., A. R. Nehrir, S. A. Kooi, J. E. Collins, R. A. Barton-Grimley, A. Notari, D. B. Harper, and J. Lee, 2022: Differential absorption lidar measurements of water vapor by the High Altitude Lidar Observatory (HALO): Retrieval framework and first results. *Atmos. Meas. Tech.*, **15**, 605–626, https://doi.org/10.5194/amt-15-605-2022.

Chen, X., L. R. Leung, Z. Feng, and Q. Yang, 2023: Environmental controls on MCS lifetime rainfall over tropical oceans. *Geophys. Res. Lett.*, **50**, e2023GL103267, https://doi.org/10.1029/2023GL103267.

Cheng, W.-Y., D. Kim, A. Rowe, Y. Moon, and S. Wang, 2020: Mechanisms of convective clustering during a 2-day rain event in AMIE/DYNAMO. *J. Adv. Model. Earth Syst.*, **12**, e2019MS001907, https://doi.org/10.1029/2019MS001907.

DeLonge, M., and J. D. Fuentes, 2012: Controls on boundary-layer thermodynamics and dynamics in coastal West Africa during the rainy season of 2006. *Bound.-Layer Meteor.*, **145**, 113–130, https://doi.org/10.1007/s10546-012-9734-5.

DeLonge, M. S., J. D. Fuentes, S. Chan, P. A. Kucera, E. Joseph, A. T. Gaye, and B. Daouda, 2010: Attributes of mesoscale convective systems at the land-ocean transition in Senegal during NASA African monsoon multidisciplinary analyses 2006. *J. Geophys. Res.*, **115**, D10213, https://doi.org/10.1029/2009JD012518.

Diallo, I., M. B. Sylla, M. Camara, and A. T. Gaye, 2013: Interannual variability of rainfall over the Sahel based on multiple regional climate models simulations. *Theor. Appl. Climatol.*, **113**, 351–362, https://doi.org/10.1007/s00704-012-0791-y.

Dieng, A. L., L. Eymard, S. M. Sall, A. Lazar, and M. Leduc-Leballeur, 2014: Analysis of strengthening and dissipating mesoscale convective systems propagating off the West African Coast. *Mon. Wea. Rev.*, **142**, 4600–4623, https://doi.org/10.1175/MWR-D-13-00388.1.

Dunion, J. P., 2011: Rewriting the climatology of the tropical North Atlantic and Caribbean Sea atmosphere. *J. Climate*, **24**, 893–908, https://doi.org/10.1175/2010JCLI3496.1.

Emanuel, K. A., J. D. Neelin, and C. S. Bretherton, 1994: On large-scale circulations in convecting atmospheres. *Quart. J. Roy. Meteor. Soc.*, **120**, 1111–1143, https://doi.org/10.1256/smsqj.51901.

Feng, Z., and Coauthors, 2021: A global high-resolution mesoscale convective system database using satellite-derived cloud tops, surface precipitation, and tracking. *J. Geophys. Res. Atmos.*, **126**, e2020JD034202, https://doi.org/10.1029/2020JD034202.

——, and Coauthors, 2025: Mesoscale Convective Systems Tracking Method Intercomparison (MCSMIP): Application to DYAMOND global km-scale simulations. *J. Geophys. Res. Atmos.*, **130**, e2024JD042204, https://doi.org/10.1029/2024JD042204.

Fink, A. H., and A. Reiner, 2003: Spatiotemporal variability of the relation between African easterly waves and West African squall lines in 1998 and 1999. *J. Geophys. Res.*, **108**, 4332, https://doi.org/10.1029/2002JD002816.

Fischer, C., A. H. Fink, E. Schömer, M. Rautenhaus, and M. Riemer, 2024: An objective identification technique for potential vorticity structures associated with African easterly waves. *Geosci. Model Dev.*, **17**, 4213–4228, https://doi.org/10.5194/gmd-17-4213-2024.

Futyan, J. M., and A. D. Del Genio, 2007: Deep convective system evolution over Africa and the tropical Atlantic. *J. Climate*, **20**, 5041–5060, https://doi.org/10.1175/JCLI4297.1.

Unauthenticated | Downloaded 10/23/26 03:43 PM UTC

Galarneau, T. J., Jr., X. Zeng, R. D. Dixon, A. Ouyed, H. Su, and W. Cui, 2023: Tropical mesoscale convective system formation environments. *Atmos. Sci. Lett.*, **24**, e1152, https://doi.org/10.1002/asl.1152.

Gelaro, R., and Coauthors, 2017: The Modern-Era Retrospective Analysis for Research and Applications, version 2 (MERRA-2). *J. Climate*, **30**, 5419–5454, https://doi.org/10.1175/JCLI-D-16-0758.1.

Guy, N., and S. A. Rutledge, 2012: Regional comparison of West African convective characteristics: A TRMM-based climatology. *Quart. J. Roy. Meteor. Soc.*, **138**, 1179–1195, https://doi.org/10.1002/qj.1865.

——, ——, and R. Cifelli, 2011: Radar characteristics of continental, coastal, and maritime convection observed during AMMA/NAMMA. *Quart. J. Roy. Meteor. Soc.*, **137**, 1241–1256, https://doi.org/10.1002/qj.839.

Hamada, A., Y. Murayama, and Y. N. Takayabu, 2014: Regional characteristics of extreme rainfall extracted from TRMM PR measurements. *J. Climate*, **27**, 8151–8169, https://doi.org/10.1175/JCLI-D-14-00107.1.

Hamilton, H. L., G. S. Young, J. L. Evans, J. D. Fuentes, and K. M. N. Ocasio, 2017: The relationship between the Guinea highlands and the West African offshore rainfall maximum. *Geophys. Res. Lett.*, **44**, 1158–1166, https://doi.org/10.1002/2016GL071170.

——, K. M. N. Ocasio, J. L. Evans, G. S. Young, and J. D. Fuentes, 2020: Topographic influence on the African easterly jet and African easterly wave energetics. *J. Geophys. Res. Atmos.*, **125**, e2019JD032138, https://doi.org/10.1029/2019JD032138.

Hersbach, H., and Coauthors, 2020: The ERA5 global reanalysis. *Quart. J. Roy. Meteor. Soc.*, **146**, 1999–2049, https://doi.org/10.1002/qj.3803.

Hodges, K. I., 1995: Feature tracking on the unit sphere. *Mon. Wea. Rev.*, **123**, 3458–3465, https://doi.org/10.1175/1520-0493(1995)123<3458:FTOTUS>2.0.CO;2.

Hollis, M. A., R. R. McCrary, J. P. Stachnik, C. Lewis-Merritt, and E. R. Martin, 2024: A global climatology of tropical easterly waves. *Climate Dyn.*, **62**, 2317–2332, https://doi.org/10.1007/s00382-023-07025-w.

Holloway, C. E., and J. D. Neelin, 2009: Moisture vertical structure, column water vapor, and tropical deep convection. *J. Atmos. Sci.*, **66**, 1665–1683, https://doi.org/10.1175/2008JAS2806.1.

Hopsch, S. B., C. D. Thorncroft, and K. R. Tyle, 2010: Analysis of African easterly wave structures and their role in influencing tropical cyclogenesis. *Mon. Wea. Rev.*, **138**, 1399–1419, https://doi.org/10.1175/2009MWR2760.1.

Houze, R. A., Jr., K. L. Rasmussen, M. D. Zuluaga, and S. R. Brodzik, 2015: The variable nature of convection in the tropics and subtropics: A legacy of 16 years of the tropical rainfall measuring mission satellite. *Rev. Geophys.*, **53**, 994–1021, https://doi.org/10.1002/2015RG000488.

Huang, B., C. Liu, V. Banzon, E. Freeman, G. Graham, B. Hankins, T. Smith, and H.-M. Zhang, 2021: Improvements of the Daily Optimum Interpolation Sea Surface Temperature (DOISST) version 2.1. *J. Climate*, **34**, 2923–2939, https://doi.org/10.1175/JCLI-D-20-0166.1.

Huffman, G. J., E. F. Stocker, D. T. Bolvin, E. J. Nelkin, and J. Tan, 2024: GPM IMERG final precipitation l3 half hourly 0.1 degree × 0.1 degree v07. National Center for Atmospheric Research, Computational and Information Systems Laboratory, accessed 23 May 2024, https://rda.ucar.edu/datasets/dsd731000/.

Janiga, M. A., and C. D. Thorncroft, 2016: The influence of African easterly waves on convection over tropical Africa and the east Atlantic. *Mon. Wea. Rev.*, **144**, 171–192, https://doi.org/10.1175/MWR-D-14-00419.1.

Jenkins, G., and Coauthors, 2010: Coastal observations of weather features in Senegal during the African monsoon multidisciplinary analysis special observing period 3. *J. Geophys. Res.*, **115**, D18108, https://doi.org/10.1029/2009JD013022.

Kavaya, M. J., J. Y. Beyon, G. J. Koch, M. Petros, P. J. Petzar, U. N. Singh, B. C. Trieu, and J. Yu, 2014: The Doppler Aerosol Wind (DAWN) airborne, wind-profiling coherent-detection lidar system: Overview and preliminary flight results. *J. Atmos. Oceanic Technol.*, **31**, 826–842, https://doi.org/10.1175/JTECH-D-12-00274.1.

Kiladis, G. N., K. H. Straub, and P. T. Haertel, 2005: Zonal and vertical structure of the Madden–Julian oscillation. *J. Atmos. Sci.*, **62**, 2790–2809, https://doi.org/10.1175/JAS3520.1.

——, C. D. Thorncroft, and N. M. J. Hall, 2006: Three-dimensional structure and dynamics of African easterly waves. Part I: Observations. *J. Atmos. Sci.*, **63**, 2212–2230, https://doi.org/10.1175/JAS3741.1.

Kingsmill, D. E., and R. A. Houze Jr., 1999: Thermodynamic characteristics of air flowing into and out of precipitating convection over the west Pacific warm pool. *Quart. J. Roy. Meteor. Soc.*, **125**, 1209–1229, https://doi.org/10.1002/qj.1999.49712555606.

Klotz, B. W., and P. Kucera, 2012: Observations of coastally transitioning West African mesoscale convective systems during NAMMA. *Int. J. Geophys.*, **2012**, 438706, https://doi.org/10.1155/2012/438706.

Kouadio, K., S. Bastin, A. Konare, and V. O. Ajayi, 2020: Does convection-permitting simulate better rainfall distribution and extreme over Guinean Coast and surroundings? *Climate Dyn.*, **55**, 153–174, https://doi.org/10.1007/s00382-018-4308-y.

Lawton, Q. A., S. J. Majumdar, K. Dotterer, C. Thorncroft, and C. J. Schreck, 2022: The influence of convectively coupled Kelvin waves on African easterly waves in a wave-following framework. *Mon. Wea. Rev.*, **150**, 2055–2072, https://doi.org/10.1175/MWR-D-21-0321.1.

mahollis3313, 2023: mahollis3313/TEW-tracks: TEW tracks Version v1. Zenodo, https://doi.org/10.5281/zenodo.10076724.

Maybee, B., and Coauthors, 2024: Wind shear effects in convection–permitting models influence MCS rainfall and forcing of tropical circulation. *Geophys. Res. Lett.*, **51**, e2024GL110119, https://doi.org/10.1029/2024GL110119.

Molinari, J., D. M. Romps, D. Vollaro, and L. Nguyen, 2012: CAPE in tropical cyclones. *J. Atmos. Sci.*, **69**, 2452–2463, https://doi.org/10.1175/JAS-D-11-0254.1.

Morrison, H., J. M. Peters, K. K. Chandrakar, and S. C. Sherwood, 2022: Influences of environmental relative humidity and horizontal scale of subcloud ascent on deep convective initiation. *J. Atmos. Sci.*, **79**, 337–359, https://doi.org/10.1175/JAS-D-21-0056.1.

Nesbitt, S. W., E. J. Zipser, and D. J. Cecil, 2000: A census of precipitation features in the tropics using TRMM: Radar, ice scattering, and lightning observations. *J. Climate*, **13**, 4087–4106, https://doi.org/10.1175/1520-0442(2000)013<4087:ACOPFI>2.0.CO;2.

Nowottnick, E. P., and Coauthors, 2024: Dust, convection, winds, and waves: The 2022 NASA CPEX-CV campaign. *Bull. Amer. Meteor. Soc.*, **105**, E2097–E2125, https://doi.org/10.1175/BAMS-D-23-0201.1.

Unauthenticated | Downloaded 10/23/26 03:43 PM UTC

Núñez Ocasio, K. M., and R. Rios-Berrios, 2023: African easterly wave evolution and tropical cyclogenesis in a pre-Helene (2006) Hindcast using the Model for Prediction Across Scales-Atmosphere (MPAS-A). *J. Adv. Model. Earth Syst.*, **15**, e2022MS003181, https://doi.org/10.1029/2022MS003181.

——, J. L. Evans, and G. S. Young, 2020: A wave-relative framework analysis of AEW–MCS interactions leading to tropical cyclogenesis. *Mon. Wea. Rev.*, **148**, 4657–4671, https://doi.org/10.1175/MWR-D-20-0152.1.

——, A. Brammer, J. L. Evans, G. S. Young, and Z. L. Moon, 2021: Favorable monsoon environment over eastern Africa for subsequent tropical cyclogenesis of African easterly waves. *J. Atmos. Sci.*, **78**, 2911–2925, https://doi.org/10.1175/JAS-D-20-0339.1.

Ogino, S.-Y., M. D. Yamanaka, S. Mori, and J. Matsumoto, 2016: How much is the precipitation amount over the tropical coastal region? *J. Climate*, **29**, 1231–1236, https://doi.org/10.1175/JCLI-D-15-0484.1.

Pereira, L. G., and S. A. Rutledge, 2006: Diurnal cycle of shallow and deep convection for a tropical land and an ocean environment and its relationship to synoptic wind regimes. *Mon. Wea. Rev.*, **134**, 2688–2701, https://doi.org/10.1175/MWR3181.1.

Peters, J. M., W. Hannah, and H. Morrison, 2019: The influence of vertical wind shear on moist thermals. *J. Atmos. Sci.*, **76**, 1645–1659, https://doi.org/10.1175/JAS-D-18-0296.1.

——, H. Morrison, T. C. Nelson, J. N. Marquis, J. P. Mulholland, and C. J. Nowotarski, 2022a: The influence of shear on deep convection initiation. Part I: Theory. *J. Atmos. Sci.*, **79**, 1669–1690, https://doi.org/10.1175/JAS-D-21-0145.1.

——, ——, ——, ——, ——, and ——, 2022b: The influence of shear on deep convection initiation. Part II: Simulations. *J. Atmos. Sci.*, **79**, 1691–1711, https://doi.org/10.1175/JAS-D-21-0144.1.

Powell, S. W., 2024: Updraft width implications for cumulonimbus growth in a moist marine environment. *J. Atmos. Sci.*, **81**, 629–648, https://doi.org/10.1175/JAS-D-23-0065.1.

Prein, A. F., and Coauthors, 2024: Km-scale simulations of mesoscale convective systems over South America—A feature tracker intercomparison. *J. Geophys. Res. Atmos.*, **129**, e2023JD040254, https://doi.org/10.1029/2023JD040254.

Rajagopal, M., J. Russell, G. Skok, and E. Zipser, 2023: Tracking mesoscale convective systems in IMERG and regional variability of their properties in the tropics. *J. Geophys. Res. Atmos.*, **128**, e2023JD038563, https://doi.org/10.1029/2023JD038563.

Redelsperger, J.-L., C. D. Thorncroft, A. Diedhiou, T. Lebel, D. J. Parker, and J. Polcher, 2006: African monsoon multidisciplinary analysis: An international research project and field campaign. *Bull. Amer. Meteor. Soc.*, **87**, 1739–1746, https://doi.org/10.1175/BAMS-87-12-1739.

Robe, F. R., and K. A. Emanuel, 2001: The effect of vertical wind shear on radiative–convective equilibrium states. *J. Atmos. Sci.*, **58**, 1427–1445, https://doi.org/10.1175/1520-0469(2001)058<1427:TEOVWS>2.0.CO;2.

Roca, R., T. Fiolleau, and D. Bouniol, 2017: A simple model of the life cycle of mesoscale convective systems cloud shield in the tropics. *J. Climate*, **30**, 4283–4298, https://doi.org/10.1175/JCLI-D-16-0556.1.

Russell, J. O. H., and A. Aiyyer, 2020: The potential vorticity structure and dynamics of African easterly waves. *J. Atmos. Sci.*, **77**, 871–890, https://doi.org/10.1175/JAS-D-19-0019.1.

Schiro, K. A., S. C. Sullivan, Y.-H. Kuo, H. Su, P. Gentine, G. S. Elsaesser, J. H. Jiang, and J. D. Neelin, 2020: Environmental controls on tropical mesoscale convective system precipitation intensity. *J. Atmos. Sci.*, **77**, 4233–4249, https://doi.org/10.1175/JAS-D-20-0111.1.

Schumacher, C., and R. A. Houze, 2006: Stratiform precipitation production over sub-Saharan Africa and the tropical east Atlantic as observed by TRMM. *Quart. J. Roy. Meteor. Soc.*, **132**, 2235–2255, https://doi.org/10.1256/qj.05.121.

Schwendike, J., and S. C. Jones, 2010: Convection in an African easterly wave over West Africa and the eastern Atlantic: A model case study of Helene (2006). *Quart. J. Roy. Meteor. Soc.*, **136**, 364–396, https://doi.org/10.1002/qj.566.

Skok, G., J. Bacmeister, and J. Tribbia, 2013: Analysis of tropical cyclone precipitation using an object-based algorithm. *J. Climate*, **26**, 2563–2579, https://doi.org/10.1175/JCLI-D-12-00135.1.

Takahashi, H., M. Lebsock, Z. J. Luo, H. Masunaga, and C. Wang, 2021: Detection and tracking of tropical convective storms based on globally gridded precipitation measurements: Algorithm and survey over the tropics. *J. Appl. Meteor. Climatol.*, **60**, 403–421, https://doi.org/10.1175/JAMC-D-20-0171.1.

——, Z. J. Luo, G. Stephens, and J. P. Mulholland, 2023: Revisiting the land-ocean contrasts in deep convective cloud intensity using global satellite observations. *Geophys. Res. Lett.*, **50**, e2022GL102089, https://doi.org/10.1029/2022GL102089.

Tao, C., S. Xie, S. Tang, J. Lee, H.-Y. Ma, C. Zhang, and W. Lin, 2023: Diurnal cycle of precipitation over global monsoon systems in CMIP6 simulations. *Climate Dyn.*, **60**, 3947–3968, https://doi.org/10.1007/s00382-022-06546-0.

Tompkins, C. F., and S. Chiao, 2012: Modeling studies of impacts from the Guinea highlands in relation to tropical cyclogenesis along the West African Coast. *Meteor. Atmos. Phys.*, **115**, 57–72, https://doi.org/10.1007/s00703-011-0167-3.

Wolding, B., J. Dias, G. Kiladis, F. Ahmed, S. W. Powell, E. Maloney, and M. Branson, 2020: Interactions between moisture and tropical convection. Part I: The coevolution of moisture and convection. *J. Atmos. Sci.*, **77**, 1783–1799, https://doi.org/10.1175/JAS-D-19-0225.1.

——, S. W. Powell, F. Ahmed, J. Dias, M. Gehne, G. Kiladis, and J. D. Neelin, 2022: Tropical thermodynamic–convection coupling in observations and reanalyses. *J. Atmos. Sci.*, **79**, 1781–1803, https://doi.org/10.1175/JAS-D-21-0256.1.

Wong, S., A. E. Dessler, N. M. Mahowald, P. Yang, and Q. Feng, 2009: Maintenance of lower tropospheric temperature inversion in the Saharan air layer by dust and dry anomaly. *J. Climate*, **22**, 5149–5162, https://doi.org/10.1175/2009JCLI2847.1.

Wu, S.-N., N. Sakaeda, E. Martin, R. Rios-Berrios, and J. Russell, 2024: The contribution of mesoscale convective systems to the coastal rainfall maximum over West Africa. *Mon. Wea. Rev.*, **152**, 1787–1802, https://doi.org/10.1175/MWR-D-23-0148.1.

Zuluaga, M. D., and R. A. Houze, 2015: Extreme convection of the near-equatorial Americas, Africa, and adjoining oceans as seen by TRMM. *Mon. Wea. Rev.*, **143**, 298–316, https://doi.org/10.1175/MWR-D-14-00109.1.

Unauthenticated | Downloaded 10/23/26 03:43 PM UTC